

Geometry of Spinning Ellis Wormholes

Xiao Yan Chew, Burkhard Kleihaus, and Jutta Kunz
Institut für Physik, Universität Oldenburg, D-26111 Oldenburg, Germany
(Dated: October 2, 2018)

We give a detailed account of the properties of spinning Ellis wormholes, supported by a phantom field. The general set of solutions depends on three parameters, associated with the size of the throat, the rotation and the symmetry of the solutions. For symmetric wormholes the global charges possess the same values in both asymptotic regions, while this is no longer the case for non-symmetric wormholes. We present mass formulae for these wormholes, study their quadrupole moments, and discuss the geometry of their throat and their ergoregion. We demonstrate, that these wormholes possess limiting configurations corresponding to an extremal Kerr black hole. Moreover, we analyze the geodesics of these wormholes, and show that they possess bound orbits.

PACS numbers: 04.20.Jb, 04.40.-b, 04.40.Nr

I. INTRODUCTION

General Relativity allows for Lorentzian wormholes [1], which can be either non-traversable or traversable. Non-traversable wormholes were first discussed in 1935 by Einstein and Rosen [2]. Here the famous ‘Einstein-Rosen bridge’ represents an interesting feature of the Schwarzschild spacetime, connecting two asymptotically flat universes by a throat. In the 1950’s Wheeler discussed the intriguing possibility to connect two distant regions within a single universe [3, 4]. Unfortunately, this kind of wormholes does not allow for their passage [5–9].

Traversable wormholes in General Relativity were first obtained by Ellis [10, 11] and Bronnikov [12] (see also [13]). However, these need the presence of a new kind of matter field coupled to gravity. Such a phantom field carries the wrong sign in front of its kinetic term, and consequently its energy-momentum tensor violates the null energy condition. The conditions for the existence of traversable wormholes as well as the properties of such static wormholes were discussed later in detail by Morris and Thorne [14], who addressed also the possibility of time-travel [15].

While phantom fields have been employed frequently in cosmology in recent years, since they give rise to an accelerated expansion of the Universe [16], it was also pointed out [17–23], that the presence of a phantom field can be evaded in the construction of wormholes, when gravity theories with higher curvature terms are considered.

Wormholes have also been considered from an astrophysical point of view, since they represent hypothetical objects that can be searched for observationally [24–26]. Cramer et al. [27] and Perlick [28], for instance, have investigated wormholes as gravitational lenses, Tsukamoto et al. have addressed the Einstein rings of wormholes [29], Bambi [30] and Nedkova et al. [31] have studied the shadow of wormholes, while Zhou et al. [32] determined the iron line profile in the X-ray reflected spectrum of a thin accretion disk around wormholes. The astrophysical signatures of mixed neutron star–wormhole systems have been addressed by Dzhunushaliev et al. [33–38].

Here we consider rotating wormholes supported by a phantom field, which represent solutions of the coupled Einstein-phantom field equations. Slowly rotating perturbative solutions of these equations were obtained by Kashargin and Sushkov [39, 40]. This was followed by a brief discussion of rapidly rotating non-perturbative wormholes given by two of us [41]. In the present paper we give a detailed account of the properties of these rotating wormholes. Moreover, we discuss rotating non-symmetric wormholes for the first time. Let us note, that the rotating wormhole metric presented by Teo [42] was not obtained as a solution of a coupled system of Einstein-matter equations.

The paper is structured as follows. We begin with the theoretical setting in section II, which includes the presentation of the action and the Ansatz, the discussion of the equations of motion and the boundary conditions, the derivation of the global charges and mass formulae as well as the derivation of the quadrupole moment. We then give a discussion of the geometric properties of the wormholes, in particular, we define the position of the throat as a minimal surface, and we demonstrate the violation of the energy conditions.

Subsequently in section III we present our numerical results for symmetric wormholes, i.e., those wormholes whose global charges are the same on both sides of the wormhole. These wormholes then possess one less parameter. In particular, we consider families of wormhole configurations for fixed equatorial throat radius, and demonstrate that these solutions approach an extremal Kerr black hole, as the angular momentum tends towards its maximal value. We then exhibit embeddings of wormhole spacetimes and demonstrate, that the Gaussian curvature of the throat turns negative at the poles, when the rotation is sufficiently fast, analogously to the curvature of the horizon of Kerr black holes. Finally, we examine the effective potential and the geodesics of rotating wormholes, which in contrast to static Ellis wormholes allow for bound orbits.

Non-symmetric rotating wormholes are presented in section IV. They depend on three parameters, and have distinct

properties when the asymmetry parameter γ is negative or positive. We analyze the domain of existence of these non-symmetric wormholes, and demonstrate that the families of non-symmetric wormholes also approach an extremal Kerr black hole. We then address the somewhat surprising fact, that the rotational velocity of the throat can exceed the velocity of light for positive γ . We show how the location of the throat changes as the asymmetry of the solutions is varied. Finally, we consider embeddings of non-symmetric wormholes and geodesics in these spacetimes. We end with our conclusions in section V, and present the metric functions for large positive asymmetry parameter in the Appendix.

II. THEORETICAL SETTING

A. Action and Ansatz

We now turn to wormhole solutions in General Relativity, obtained with a phantom field ψ . The corresponding action reads

$$S = \frac{1}{16\pi G} \int d^4x \sqrt{-g} (R + 2g^{\mu\nu} \partial_\mu \psi \partial_\nu \psi) , \quad (1)$$

leading to the Einstein equations

$$R_{\mu\nu} = -2\partial_\mu \psi \partial_\nu \psi , \quad (2)$$

and the phantom field equation

$$\partial_\mu (\sqrt{-g} g^{\mu\nu} \partial_\nu \psi) = 0 . \quad (3)$$

To construct stationary rotating spacetimes we employ the line element

$$ds^2 = -e^f dt^2 + p^2 e^{-f} \left(e^\nu [d\eta^2 + h d\theta^2] + h \sin^2 \theta (d\phi - \omega dt)^2 \right) , \quad (4)$$

where f , p , ν and ω are functions only of η and θ , and $h = \eta^2 + \eta_0^2$ is an auxiliary function. We note that the coordinate η takes positive and negative values, i.e. $-\infty < \eta < \infty$. The limits $\eta \rightarrow \pm\infty$ correspond to two distinct asymptotically flat regions. The phantom field ψ also depends only on the coordinates η and θ .

B. Equations of Motion and Boundary Conditions

When we substitute the above Ansatz into the general set of equations of motion we obtain a system of non-linear partial differential equations (PDEs). As observed in [41] the PDE for the function p decouples, and has the simple form

$$p_{,\eta,\eta} + \frac{3\eta}{h} p_{,\eta} + \frac{2 \cos \theta}{h \sin \theta} p_{,\theta} + \frac{1}{h} p_{,\theta,\theta} = 0 . \quad (5)$$

A solution which satisfies the boundary conditions $p(\eta \rightarrow \infty) = p(\eta \rightarrow -\infty) = 1$ and $\partial_\theta p(\theta = 0) = \partial_\theta p(\theta = \pi) = 0$ is given by

$$p = 1 . \quad (6)$$

Consequently, we obtain the phantom field equation

$$\partial_\eta (h \sin \theta \partial_\eta \psi) + \partial_\theta (\sin \theta \partial_\theta \psi) = 0 . \quad (7)$$

A first integral can be obtained under the assumption $\partial_\theta \psi = 0$,

$$\partial_\eta \psi = \frac{D}{h} , \quad (8)$$

where D denotes the phantom scalar charge. This leads to the closed form solution for ψ

$$\psi = D (\arctan(\eta/\eta_0) - \pi/2) , \quad (9)$$

where the integration constant was chosen to satisfy $\psi(\infty) = 0$.

We now turn to the Einstein equations. With $p = 1$ and $\partial_\theta \psi = 0$ the equations $R_{\phi\phi} = 0$, $R_{\theta\theta} = 0$, $R_{t\phi} = 0$, $R_{tt} = 0$ and $R_{\eta\theta} = 0$ are independent of the scalar field. They yield three second order PDEs for the functions f , ω and ν , and a constraint,

$$0 = \partial_\eta (h \sin \theta \partial_\eta f) + \partial_\theta (\sin \theta \partial_\theta f) - h \sin^3 \theta e^{-2f} (h(\partial_\eta \omega)^2 + (\partial_\theta \omega)^2) , \quad (10)$$

$$0 = \partial_\eta (h^2 \sin^3 \theta e^{-2f} \partial_\eta \omega) + \partial_\theta (h \sin^3 \theta e^{-2f} \partial_\theta \omega) , \quad (11)$$

$$0 = \partial_\eta (h \sin \theta \partial_\eta \nu) + \sin \theta \partial_{\theta\theta} \nu - \cos \theta \partial_\theta \nu - h \sin^3 \theta e^{-2f} (h(\partial_\eta \omega)^2 - 2(\partial_\theta \omega)^2) , \quad (12)$$

$$0 = -h \sin \theta \partial_\eta f \partial_\theta f + h \cos \theta \partial_\eta \nu + \eta \sin \theta \partial_\theta \nu + h^2 \sin^3 \theta e^{-2f} \partial_\eta \omega \partial_\theta \omega . \quad (13)$$

In order to obtain regular solutions we have to impose boundary conditions in the asymptotic regions $\eta \rightarrow \pm\infty$ and on the axis $\theta = 0, \pi$. For $\eta \rightarrow +\infty$ we require the metric to approach Minkowski spacetime, i.e.,

$$f|_{\eta \rightarrow \infty} = 0 , \quad \omega|_{\eta \rightarrow \infty} = 0 , \quad \nu|_{\eta \rightarrow \infty} = 0 . \quad (14)$$

In the limit $\eta \rightarrow -\infty$ we allow for finite values of the functions f and ω ,

$$f|_{\eta \rightarrow -\infty} = \gamma , \quad \omega|_{\eta \rightarrow -\infty} = \omega_{-\infty} , \quad \nu|_{\eta \rightarrow -\infty} = 0 . \quad (15)$$

We refer to the solutions as symmetric, when $\gamma = 0$, and non-symmetric, when $\gamma \neq 0$. Note, that in the limit $\eta \rightarrow -\infty$ the spacetime becomes Minkowskian after a suitable coordinate transformation is performed. Regularity on the symmetry axis requires

$$\partial_\theta f|_{\theta=0} = 0 , \quad \partial_\theta \omega|_{\theta=0} = 0 , \quad \nu|_{\theta=0} = 0 , \quad (16)$$

together with the analogous conditions at $\theta = \pi$.

Static wormhole solutions correspond to $\omega_{-\infty} = 0$. They are known in closed form,

$$f = \frac{\gamma}{2} \left(1 - \frac{2}{\pi} \arctan \left(\frac{\eta}{\eta_0} \right) \right) , \quad \omega = 0 , \quad \nu = 0 . \quad (17)$$

Rotating wormhole solutions of the above equations have been studied in [41] for the symmetric case only, while we here address the non-symmetric case, as well. Substitution of the solutions for f , ω and ν in $R_{\eta\eta}$ shows, that

$$R_{\eta\eta} = -2 \frac{D^2}{h^2} , \quad (18)$$

where the scalar charge D depends on the mass and the angular momentum of the spacetime. Explicitly we find

$$D^2 = \frac{h}{4} [h(\partial_\eta f)^2 - (\partial_\theta f)^2] - \frac{h}{2} \left(\eta \partial_\eta \nu - \frac{\cos \theta}{\sin \theta} \partial_\theta \nu \right) - \frac{h^2}{4} \sin^2 \theta e^{-2f} [h(\partial_\eta \omega)^2 - (\partial_\theta \omega)^2] + \eta_0^2 . \quad (19)$$

C. Mass, Angular Momentum and Mass Formulae

The mass and angular momentum of the wormhole solutions are engraved in the asymptotic form of the metric tensor. For an asymptotically flat metric, the mass and the angular momentum can be read off from the components g_{tt} and $g_{t\varphi}$,

$$g_{tt} \xrightarrow{\eta \rightarrow \pm\infty} - \left(1 \mp \frac{2\mu_\pm}{\eta} \right) , \quad g_{t\varphi} \xrightarrow{\eta \rightarrow \pm\infty} - \frac{2J_\pm \sin^2 \theta}{\eta} . \quad (20)$$

In the limit $\eta \rightarrow +\infty$ the wormhole metric becomes Minkowskian, as seen from the asymptotic behavior of the metric functions. In particular,

$$f \rightarrow -\frac{2\mu_+}{\eta} , \quad \omega \rightarrow \frac{2J_+}{\eta^3} , \quad \text{as } \eta \rightarrow +\infty , \quad (21)$$

so we can read off the mass μ_+ and the angular momentum J_+ directly.

The analogous asymptotic expansion at the other side of the wormhole reads

$$f \rightarrow \gamma + \frac{2\mu_-}{\eta}, \quad \omega \rightarrow \omega_{-\infty} + \frac{2J_-}{\eta^3}, \quad \text{as } \eta \rightarrow -\infty. \quad (22)$$

However, in order to identify the mass $\bar{\mu}_-$ and the angular momentum \bar{J}_- at $\eta \rightarrow -\infty$, we first have to perform a coordinate transformation to obtain an asymptotically flat spacetime in this limit. After applying

$$\bar{t} = e^{\gamma/2}t, \quad \bar{\eta} = e^{-\gamma/2}\eta, \quad \bar{\phi} = \phi - \omega_{-\infty}t, \quad (23)$$

we obtain $\bar{\mu}_-$ and \bar{J}_- in terms of the parameters μ_- and J_- ,

$$\bar{J}_- = J_- e^{-2\gamma}, \quad \bar{\mu}_- = \mu_- e^{-\gamma/2}. \quad (24)$$

Let us now derive some relations between the global charges. We first note that Eq. (11) is in the form of a conservation law, and integrate Eq. (11) over the full range of η and θ , $-\infty < \eta < \infty$, $0 < \theta < \pi$. This leads to

$$\int_0^\pi [h^2 e^{-2f} \sin^3 \theta \omega, \eta]_{\eta \rightarrow \infty} d\theta = \int_0^\pi [h^2 e^{-2f} \sin^3 \theta \omega, \eta]_{\eta \rightarrow -\infty} d\theta. \quad (25)$$

Inserting the asymptotic expansions for ω and f , Eqs. (21)-(22), we find

$$J_+ = e^{-2\gamma} J_- = \bar{J}_-. \quad (26)$$

Thus the angular momenta on both sides of the wormhole are equal.

To derive a second relation, we multiply Eq. (11) by ω and subtract it from Eq. (10). This yields again an equation in the form of a conservation law,

$$\partial_\eta (h \sin \theta [\partial_\eta f - e^{-2f} h \sin^2 \theta \omega \partial_\eta \omega]) + \partial_\theta (\sin \theta [\partial_\theta f - e^{-2f} h \sin^2 \theta \omega \partial_\theta \omega]) = 0. \quad (27)$$

Integrating Eq. (27) and taking into account the asymptotic expansions Eqs. (21)-(22), we find

$$\mu_+ + \mu_- = 2\omega_{-\infty} e^{-2\gamma} J_- = 2\omega_{-\infty} J_+. \quad (28)$$

For the static wormhole solutions (17), this relation reduces to $\mu_+ = -\mu_-$, where the mass μ_+ is related to γ by $\mu_+ = \gamma \eta_0 / 2\pi$.

In the symmetric case, we regain a mass formula akin to the Smarr formula for black holes. Here we integrate both formulae from the throat ($\eta = 0$) to infinity, and take into account that $\partial_\eta f$ vanishes at the throat. Denoting $\omega(0) = \omega_0$, we find [41]

$$\mu_+ = \omega_{-\infty} J_+ = 2\omega_0 J_+, \quad (29)$$

where $\omega_{-\infty} = 2\omega_0$ follows from the symmetry and the choice of boundary conditions. Consequently, also the relation $\mu_- = 2\omega_0 J_-$ holds in this case. Thus on both sides of the wormhole the mass is the same. Note, that the mass relation (29) then agrees with the one for extremal Kerr black holes, when ω_0 is identified with the horizon angular velocity.

To find a relation of D^2 to the mass we evaluate Eq. (19) in the limit $\eta \rightarrow \infty$. Here we must take into account the asymptotic behaviour of the function ν ,

$$\nu \rightarrow -c_2 \frac{\sin^2 \theta}{\eta^2}. \quad (30)$$

This yields

$$c_2 = \mu_+^2 + \eta_0^2 - D^2, \quad (31)$$

which reduces to $0 = \mu_+^2 + \eta_0^2 - D^2$ in the static case.

D. Quadrupole Moment

In order to extract the quadrupole moment Q of the rotating wormhole solutions, we need to consider the expansion of the metric in the asymptotic regions. For simplicity, let us only consider $\eta \rightarrow +\infty$ here. The asymptotic expansion of the metric functions is then given by

$$f = -\frac{2\mu_+}{\eta} + \frac{2}{3} \frac{\mu_+ \eta_0^2}{\eta^3} + \frac{2}{3} \frac{2\mu_+ \eta_0^2 - 3f_3}{\eta^3} P_2(\cos \theta) + \mathcal{O}(\eta^{-4}), \quad (32)$$

$$\nu = -c_2 \frac{\sin^2 \theta}{\eta^2} + \mathcal{O}(\eta^{-3}), \quad (33)$$

$$\omega = 2 \frac{J_+}{\eta^3} + \mathcal{O}(\eta^{-4}), \quad (34)$$

where $P_2(\cos \theta)$ is the second Legendre polynomial and f_3 and c_2 are constants.

The quadrupole moment can now be derived employing the definitions of Geroch and Hansen [43, 44], and following later work [45–47] according to the steps outlined in [48] we first transform the metric to quasi-isotropic coordinates. This yields

$$ds^2 = -e^f dt^2 + \left(1 + \frac{r_0^2}{r^2}\right)^2 e^{-f} [e^\nu (dr^2 + r^2 d\theta^2) + r^2 \sin^2 \theta (d\phi - \omega dt)^2], \quad (35)$$

where r is related to η by $\eta/\eta_0 = (r/r_0 - r_0/r)/2$, and $r_0 = \eta_0/2$. We compare this with

$$ds^2 = -e^{2\nu_0} dt^2 + e^{2(\nu_1 - \nu_0)} [e^{2\nu_2} (dr^2 + r^2 d\theta^2) + r^2 \sin^2 \theta (d\phi - \omega dt)^2] \quad (36)$$

and identify

$$\nu_0 = f/2, \quad e^{\nu_1} = 1 + \frac{r_0^2}{r^2}, \quad \nu_2 = \nu/2. \quad (37)$$

Using the expansion $\eta^{-1} = r^{-1}(1 + (r/r_0)^{-2} + \mathcal{O}((r/r_0)^{-4}))$ in the asymptotic region we find by comparison with Eqs. (A9)-(A11) in [48]

$$\begin{aligned} \nu_0 &= -\frac{\mu_+}{r} + \frac{1}{12} \frac{\mu_+ \eta_0^2}{r^3} + \frac{2\mu_+ \eta_0^2 - 3f_3}{3r^3} P_2(\cos \theta) + \mathcal{O}(r^{-4}) \\ &= -\frac{\mu_+}{r} + \frac{1}{3} \frac{d_1 \mu_+}{r^3} - \frac{M_2}{r^3} P_2(\cos \theta) + \mathcal{O}(r^{-4}), \end{aligned} \quad (38)$$

$$\begin{aligned} \nu_1 &= \frac{\eta_0^2}{4r^2} + \mathcal{O}(r^{-3}) \\ &= \frac{d_1}{r^2} + \mathcal{O}(r^{-3}), \end{aligned} \quad (39)$$

$$\begin{aligned} \nu_2 &= -c_2 \frac{\sin^2 \theta}{2r^2} + \mathcal{O}(r^{-3}) \\ &= -\frac{4\mu_+^2 + 16d_1 - q_2}{8r^2} \sin^2 \theta + \mathcal{O}(r^{-3}), \end{aligned} \quad (40)$$

where we have slightly changed the notation of [48]: $D_1 \rightarrow d_1$, $q^2 \rightarrow -q_2$. Now d_1 , q_2 and M_2 can be expressed in terms of f_3 and c_2 ,

$$d_1 = \frac{\eta_0^2}{4}, \quad q_2 = 4(\mu_+^2 + \eta_0^2 - c_2) = 4D^2, \quad M_2 = f_3 - \frac{2\mu_+ \eta_0^2}{3}. \quad (41)$$

Thus we finally arrive at the quadrupole moment

$$Q = -f_3 + \mu_+ \eta_0^2 + \frac{\mu_+ (\mu_+^2 - D^2)}{3} \quad (42)$$

(see e.g. [48] for more details).

E. Geometric Properties

Let us next address the geometric properties of the wormhole solutions. We first consider the equatorial (or circumferential) radius $R_e(\eta)$ as a function of the radial coordinate

$$R_e(\eta) = \sqrt{\eta^2 + \eta_0^2} \left[e^{-f/2} \right]_{\theta=\pi/2} . \quad (43)$$

Because of the rotation, the throat of the wormholes should deform and its circumference should be largest in the equatorial plane. Therefore a study of $R_e(\eta)$ should reveal the location of the throat in the equatorial plane.

Consequently, we define the throat of the wormhole as the surface of minimal area, which intersects the equatorial plane at the circle of minimal circumferential radius R_e , i.e.,

$$R_e = \min_{-\infty \leq \eta \leq \infty} \left\{ \sqrt{h} e^{-f/2} \Big|_{\theta=\pi/2} \right\} , \quad (44)$$

for the line element Eq. (4).

We now parametrize the surface of the throat by $(\eta_t(\theta), \theta, \varphi)$. Then the line element on the surface reads

$$d\sigma^2 = e^{-f+\nu} [\eta_t'^2 + h] d\theta^2 + e^{-f} h \sin^2 \theta d\varphi^2 , \quad (45)$$

where we defined $\eta_t' = d\eta_t/d\theta$, and the functions f , ν and h are regarded as functions of η_t and θ . The area of the surface is now given by the integral of the square root of the determinant of the metric tensor

$$A_\sigma = \int L_\sigma d\theta d\varphi \quad (46)$$

with

$$L_\sigma = \sqrt{\eta_t'^2 + h} \sqrt{h} \sin \theta e^{-f+\nu/2} . \quad (47)$$

The function $\eta_t(\theta)$ is determined as solution of the Euler-Lagrange equation

$$\frac{d}{d\theta} \frac{\partial L_\sigma}{\partial \eta_t'} - \frac{\partial L_\sigma}{\partial \eta_t} = 0 . \quad (48)$$

This yields the ordinary differential equation

$$\eta_t'' + h \partial_{\eta_t} s - 2\eta_t - \left[\partial_\theta s - \frac{\cos \theta}{\sin \theta} \right] \eta_t' + \left[\partial_{\eta_t} s - \frac{3\eta_t}{h} \right] \eta_t'^2 - \left[\partial_\theta s - \frac{\cos \theta}{\sin \theta} \right] \frac{1}{h} \eta_t'^3 = 0 , \quad (49)$$

where we introduced $s = f - \nu/2$. We solve this equation numerically for boundary conditions $\eta_t'(0) = 0$, required by regularity, and $\eta_t(\pi/2) = \eta_e$, where η_e is the coordinate of the throat in the equatorial plane, determined by the minimum condition for the circumferential radius.

We note that in the symmetric case the throat is located at the constant coordinate $\eta_t = 0$, since $\eta_e = 0$ and $\partial_{\eta_t} s = 0$ at $\eta = 0$ for all θ . For the static wormholes $\nu = 0$ and $\partial_\theta f = 0$. In this case the minimum condition Eq. (44) yields $h \partial_{\eta_t} f - 2\eta_e = 0$, which implies $h \partial_{\eta_t} s - 2\eta_e = 0$ in Eq. (49). Consequently the solution of Eq. (49) is in this case $\eta_t = \eta_e$. Therefore the static non-symmetric wormholes also possess a throat with constant coordinate (as expected). For the rotating non-symmetric wormholes, however, it is not obvious, that the throat should be located at a constant radial coordinate, as well. Therefore the dependence of the coordinate η_t on θ must be examined numerically. We further note, that we do not find rotating Ellis wormhole solutions with multiple throats, separated by bellies (or equators).

To gain further information on the geometry of the rotating symmetric wormholes, we consider in addition the polar radius R_p

$$R_p = \frac{\eta_0}{\pi} \int_0^\pi e^{(\nu-f)/2} \Big|_{\eta=0} d\theta , \quad (50)$$

and the areal radius R_A

$$R_A^2 = \frac{\eta_0^2}{2} \int_0^\pi e^{\nu/2-f} \Big|_{\eta=0} \sin \theta d\theta . \quad (51)$$

Denoting the angular velocity of the throat by $\Omega = \omega_0$, the rotational velocity of the throat in the equatorial plane is given by

$$v_e = R_e \Omega . \quad (52)$$

It was shown in [41] that $v_e \leq 1$ for the symmetric wormholes.

F. Violation of the Null Energy Condition

Let us next demonstrate the violation of the Null Energy Condition (NEC) and consider the quantity

$$\Xi = R_{\mu\nu}k^\mu k^\nu, \quad (53)$$

with null vector [40]

$$k^\mu = \left(e^{-f/2}, e^{f/2-\nu/2}, 0, \omega e^{-f/2} \right). \quad (54)$$

Taking into account the Einstein equations and the phantom field equation we obtain

$$\Xi = -2D^2 \frac{e^{f-\nu}}{h^2}. \quad (55)$$

Since Ξ is non-positive the NEC is violated everywhere. In order to obtain a global scale invariant quantity as measure of the NEC violation we define for later reference for the symmetric wormholes

$$Y = \frac{1}{R_e} \int \Xi \sqrt{-g} d\eta d\theta d\varphi = -8\pi \frac{D^2}{R_e} \int_0^\infty \frac{d\eta}{\eta^2 + \eta_0^2} = -4\pi^2 \frac{D^2}{R_e \eta_0}. \quad (56)$$

III. SYMMETRIC WORMHOLES

In the following we present the properties of symmetric rotating wormhole solutions in General Relativity, which are characterized by $\gamma = 0$ [41]. We then continue with the non-symmetric case, where for fixed η_0 the solutions depend on the parameters γ and $\omega_{-\infty}$.

A. Global Charges

Symmetric rotating Ellis wormholes depend on the throat parameter η_0 and the angular velocity of the throat ω_0 . Let us first fix the throat parameter $\eta_0 = 1$ and vary ω_0 , starting from the static Ellis wormhole. Then the mass μ_+ and angular momentum J_+ increase from their Ellis value of zero with increasing angular velocity. At the same time, the rotational velocity v_e of the throat in the equatorial plane increases as it should, since it is proportional to ω_0 . The centrifugal force causes in addition an increase of the equatorial circumferential radius of the throat R_e and thus of v_e .

We exhibit in Fig. 1 the dependence of the mass μ_+ and the angular momentum J_+ on the rotational velocity v_e for these wormholes. As the rotational velocity v_e tends to its limiting value of one, where the throat would be rotating with the velocity of light the mass and the angular momentum both diverge. Also shown in Fig. 1 is the dependence of the scalar charge D (we have chosen D to be non-negative) on the rotational velocity v_e , and the relation between ω_0 and v_e .

The scalar charge is maximal for static wormholes and decreases monotonically to zero, as the family of wormhole solutions approaches its limiting configuration, where the rotational velocity reaches the speed of light. The angular velocity of the throat, however, does not increase monotonically with v_e . Instead, it reaches a maximal value and then decreases again towards zero. The reason for the occurrence of two branches with respect to ω_0 is our use of ‘isotropic’ coordinates. The analogous pattern arises for rotating black holes, when the isotropic horizon radius is held fixed, while the angular momentum increases monotonically (see e.g. [49]).

To get a more physical picture of the families of symmetric rotating wormholes and better understand the limiting behavior for $v_e \rightarrow 1$, let us now fix the equatorial throat radius R_e . Then the family of symmetric rotating wormholes evolves from the static Ellis wormhole with $\mu_+/R_e = J_+/R_e^2 = 0$ to a limiting configuration with $\mu_+/R_e = J_+/R_e^2 = 1/2$. This is seen in Fig. 2, where the scaled mass μ_+/R_e , the scaled angular momentum J_+/R_e^2 and the scaled scalar charge D/R_e are shown versus the rotational velocity v_e of the throat in the equatorial plane. Again, the scalar charge decreases monotonically and tends to zero for $v_e \rightarrow 1$. By exhibiting the r.h.s. of Eq. (29) as well, we demonstrate, that all solutions satisfy the Smarr-type relation (29) with high accuracy. Also shown in Fig. 2 are the corresponding quantities for the Kerr black holes for fixed equatorial horizon radius, $\mu/R_e = 1/2$, $J/R_e^2 = v_e/(1+v_e^2)$ and $\omega_H J/R_e = v_e^2/(1+v_e^2)$.

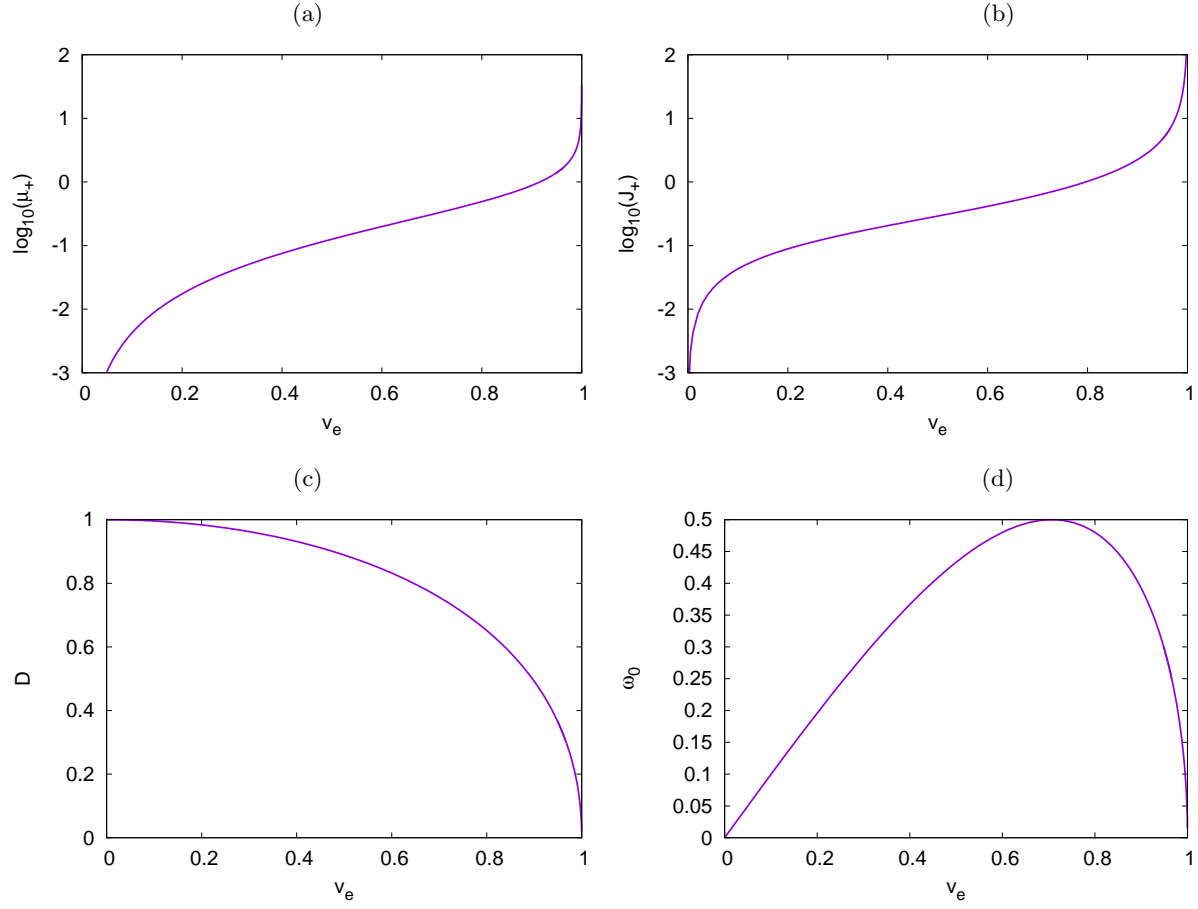


Figure 1: Properties of symmetric rotating wormholes at fixed throat parameter $\eta_0 = 1$: the mass μ_+ (a), the angular momentum J_+ (b), the scalar charge D (c), and the angular velocity of the throat ω_0 (d) versus the rotational velocity v_e of the throat in the equatorial plane.

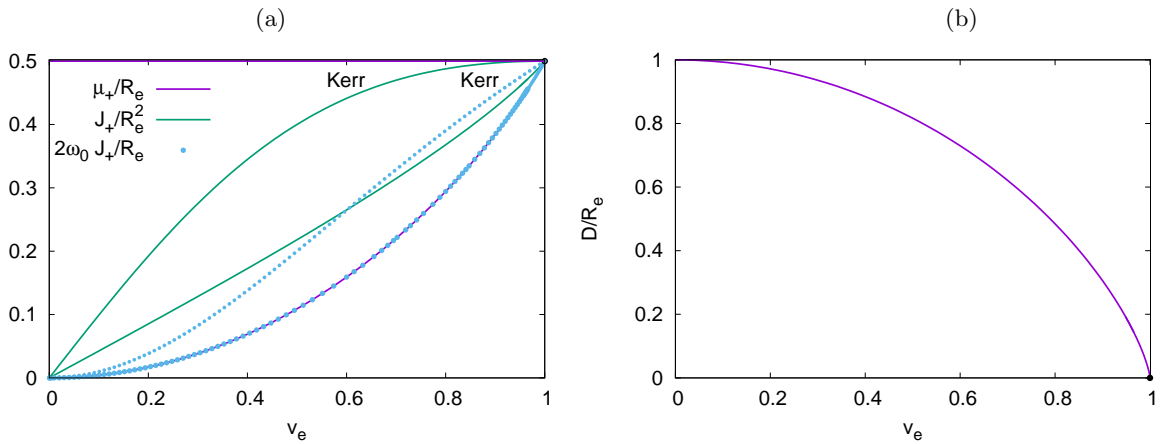


Figure 2: Properties of symmetric rotating wormholes at fixed equatorial throat radius R_e : the scaled mass μ_+/R_e , the scaled angular momentum J_+/R_e^2 and the quantity $2\omega_0 J_+/R_e$ (a), the scaled scalar charge D/R_e (b) versus the rotational velocity v_e of the throat in the equatorial plane. Also shown are the respective curves for the Kerr black holes, while the black dots mark the respective extremal Kerr values.

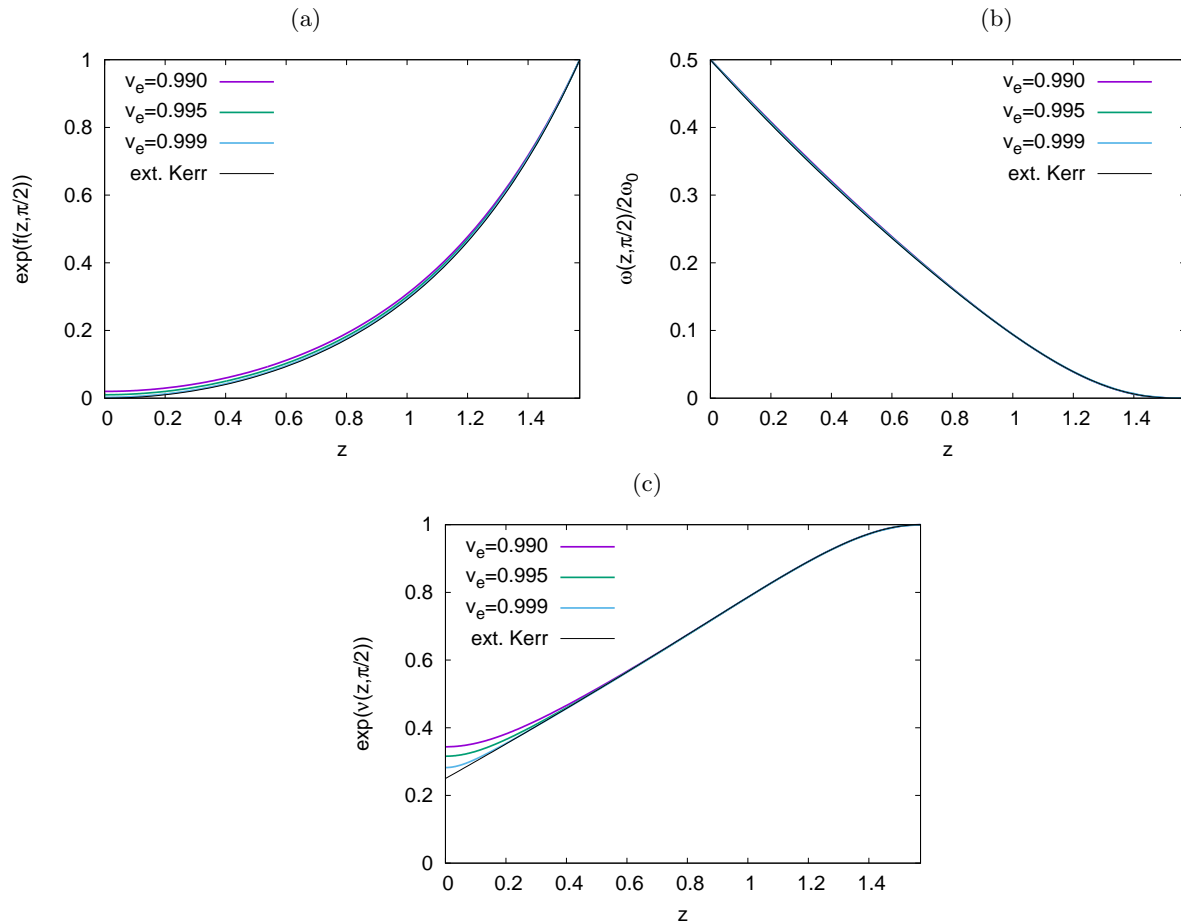


Figure 3: Properties of symmetric rotating wormholes at fixed angular velocity $\omega(0, \pi/2) = 1/2$: the limiting $v_e \rightarrow 1$ behavior of the metric functions f (a), $\omega/(2\omega_0)$ (b) and ν (c) versus the radial coordinate $z = \arctan(2\omega_0\eta)$ in the equatorial plane $\theta = \pi/2$ for three values of the rotational velocity of the throat in the equatorial plane, $v_e = 0.990, 0.995, 0.999$. The respective functions of the extremal Kerr solution with horizon angular velocity $\omega_H = 1/2$ are also shown.

B. Limit $v_e \rightarrow 1$

Let us now demonstrate, that in the limit $v_e \rightarrow 1$ an extremal Kerr black hole is approached. We will consider $\eta \geq 0$ only; the discussion for $\eta \leq 0$ is analogous. First of all, the global charges mass and angular momentum precisely assume the respective Kerr values in the limit, while the scalar charge vanishes. (Note, that a circumferential radius $R_e = 2$ corresponds to a Boyer-Lindquist horizon radius $r_H = 1$, and an extremal black hole has $\mu = J/\mu = r_H$.) Thus asymptotically the extremal Kerr metric is approached. However, in the limit $v_e \rightarrow 1$ the metric tends not only asymptotically but everywhere to the extremal Kerr metric. This is demonstrated in Fig. 3. Here we fix the angular velocity of the throat and the horizon, $\omega_0 = \omega_H = 1/2$. This requires a scaling of the radial coordinate $\eta \rightarrow 2\omega_0\eta/\eta_0$ and metric function $\omega \rightarrow \omega/(2\omega_0)$, which leaves the product $\omega\eta$ and v_e invariant. Then the metric functions f , ω and ν are shown versus the radial coordinate $z = \arctan(2\omega_0\eta)$ for $\theta = \pi/2$ and $v_e = 0.990, 0.995, 0.999$ together with the limiting extremal Kerr solution.

As the dimensionless rotational velocity v_e reaches its maximal value, $v_e = 1$, the hypersurface $\eta = 0$, which corresponds to the throat of the wormholes, must change its character. Since the limiting solution represents an extremal black hole, a degenerate horizon must form instead. Moreover, the phantom field vanishes identically in this limit, as it should for a Kerr black hole. Consequently, the Smarr relation (29) for extremal Kerr black holes is recovered, with ω_0 denoting the horizon angular velocity.

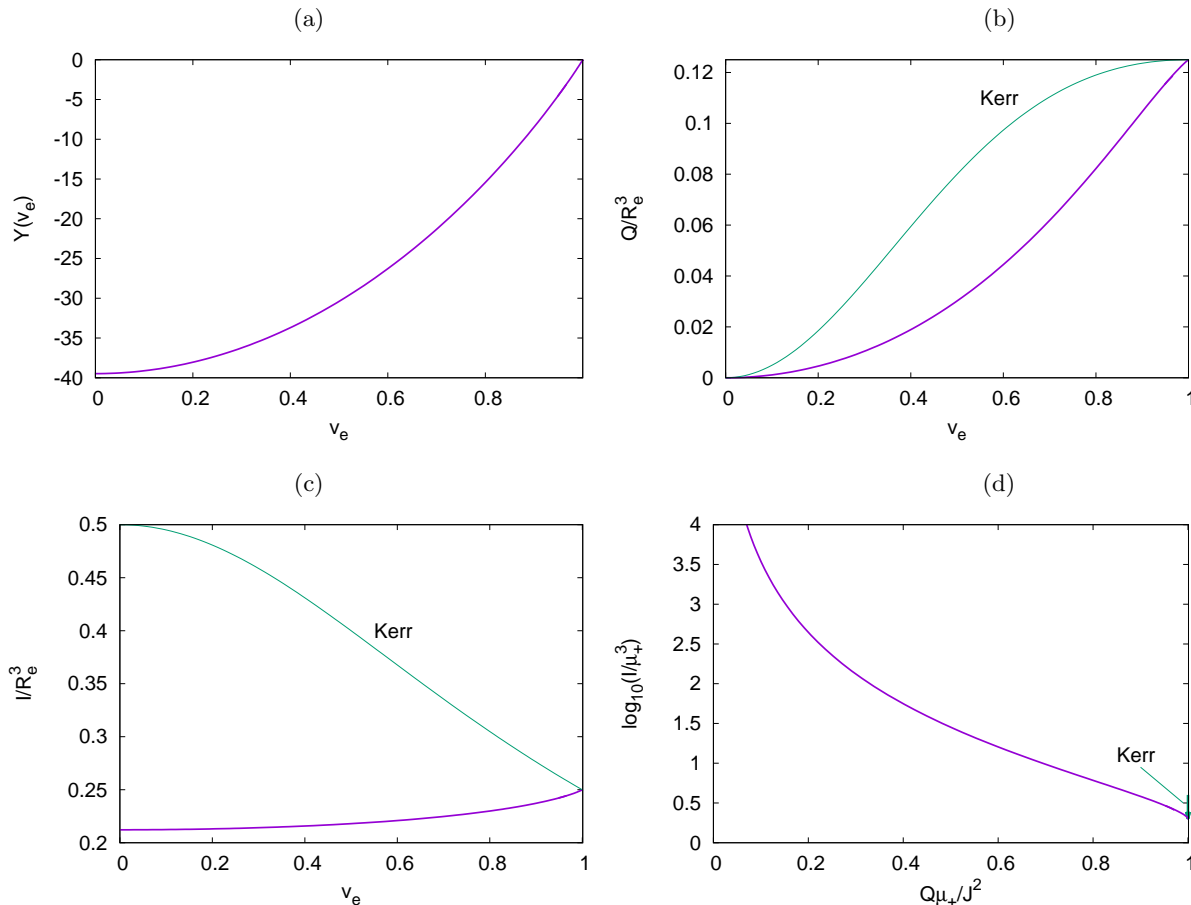


Figure 4: Properties of symmetric rotating wormholes at fixed equatorial throat radius R_e : The quantity Y , Eq. (55), giving a measure for the violation of the NEC (a), the scaled quadrupole moment Q/R_e^3 (b), and the scaled moment of inertia I/R_e^3 (c) versus the rotational velocity v_e of the throat in the equatorial plane; the dimensionless moment of inertia I/μ_+^3 versus the dimensionless quadrupole moment $Q\mu_+/J^2$ (d). Also shown are the respective curves for the Kerr black holes.

C. NEC, Quadrupole Moment and Moment of Inertia

In Fig. 4 we show the quantity Y , Eq. (55), which gives for the symmetric rotating wormhole solutions a scale independent measure for the violation of the NEC, as a function of the rotational velocity of the throat v_e . We observe that the violation of the NEC is strongest in the static limit $v_e = 0$ and disappears in the limit $v_e = 1$, where the extremal Kerr solution is approached.

The observation that with increasing rotation the violation of the NEC decreases and the family of rotating wormholes ends in an extremal black hole, appears to be a generic feature. It was also observed for rotating Ellis wormholes in 5 dimensions, which end in an extremal Myers-Perry black hole [50]. Moreover, the family of electrically charged static Ellis wormholes in 4 dimensions ends in an extremal Reissner-Nordström black hole with increasing electric charge [51].

Let us now turn to the quadrupole moment Q , given in Eq. (42), as obtained by following the procedure of Geroch and Hansen [43, 44] by extracting it from the asymptotic expansion in appropriate coordinates (see e.g. [48, 52]). We exhibit the quadrupole moment in Fig. (4) for the family of symmetric rotating wormholes at fixed equatorial throat radius R_e . Starting from zero in the static case, the scaled quadrupole moment Q/R_e^3 increases monotonically to its maximum of $Q/R_e^3 = 1/8$, when the throat velocity v_e approaches the speed of light. Also shown is the scaled quadrupole moment for the Kerr black holes, $Q/R_e^3 = (v_e/(1+v_e^2))^2/2$. We note that the scaled quadrupole moment is larger for the Kerr black holes for any value of the horizon resp. throat velocity v_e (except for $v_e = 0$ and $v_e = 1$, where both coincide).

One often considers the dimensionless quadrupole moment $Q\mu/J^2$, which is constant for the Kerr solutions, $Q\mu/J^2 = 1$. The dimensionless quadrupole moment $Q\mu_+/J_+^2$ of the wormhole solutions increases monotonically

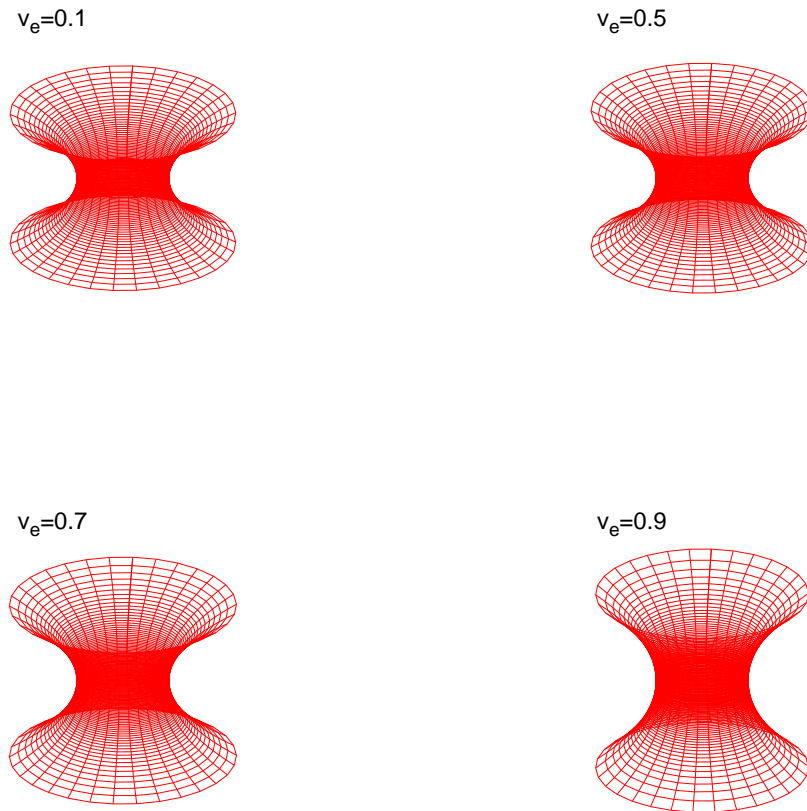


Figure 5: Properties of symmetric rotating wormholes at fixed equatorial throat radius $R_e = 2$: isometric embeddings of the equatorial plane for rotational velocities $v_e = 0.1, 0.5, 0.7$, and 0.9 .

from zero in the static limit to the value of the Kerr solutions in the limit $v_e \rightarrow 1$.

The moment of inertia $I = J_+/\omega_0$ of the wormholes is another quantity of interest, in particular, in comparison with other compact objects. We exhibit the moment of inertia I for the same set of solutions in Fig. 4. The scaled moment of inertia I/R_e^3 is smaller than the corresponding value of the Kerr black holes, $I/R_e^3 = 1/(2(1+v_e^2))$, except in the extremal limit, when they are equal.

The dimensionless moment of inertia $J_+ / (\omega_0 \mu_+^3)$ is also exhibited in Fig. 4, but now versus the dimensionless quadrupole moment $Q\mu_+ / J_+^2$. For comparison, the Kerr solutions are also included, where $J / (\Omega_H \mu^3) = 2(1 + \sqrt{1 - j^2})$ with $j = J/\mu^2$. Forming the vertical line at $|Q\mu/J^2| = 1$, they range from $J / (\Omega_H \mu^3) = 2$ in the extremal rotating case to $J / (\Omega_H \mu^3) = 4$, when the limit $J \rightarrow 0$ is taken. In contrast, for rotating wormholes, the dimensionless moment of inertia I/μ_+^3 diverges in the limit $J_+ \rightarrow 0$, since in the static limit the wormhole mass vanishes, $\mu_+ \rightarrow 0$.

D. Geometry and Ergoregion

The shape of wormholes can be visualized with the help of embedding diagrams. Let us consider the wormhole metric at fixed t in the equatorial plane, $\theta = \pi/2$ and embed it isometrically in Euclidean space

$$ds^2 = e^{-f+\nu} d\eta^2 + e^{-f} h d\phi^2 = d\rho^2 + \rho^2 d\phi^2 + dz^2, \quad (57)$$

with $\rho = \rho(\eta)$, $z = z(\eta)$. Comparison yields

$$\left(\frac{d\rho}{d\eta}\right)^2 + \left(\frac{dz}{d\eta}\right)^2 = e^{-f+\nu}, \quad \rho^2 = e^{-f} h, \quad (58)$$

which leads to $z(\eta)$. We exhibit examples of such embedding diagrams in Fig. 5 for symmetric rotating wormholes at fixed equatorial throat radius $R_e = 2$ with increasing rotational velocities $v_e = 0.1, 0.5, 0.7$, and 0.9 .

We can also try to visualize the shape of the throat, i.e., the deformation of the hypersurface $\eta = 0$. For that end we try to embed this hypersurface in a Euclidean space. However, it is known for Kerr black holes, that beyond

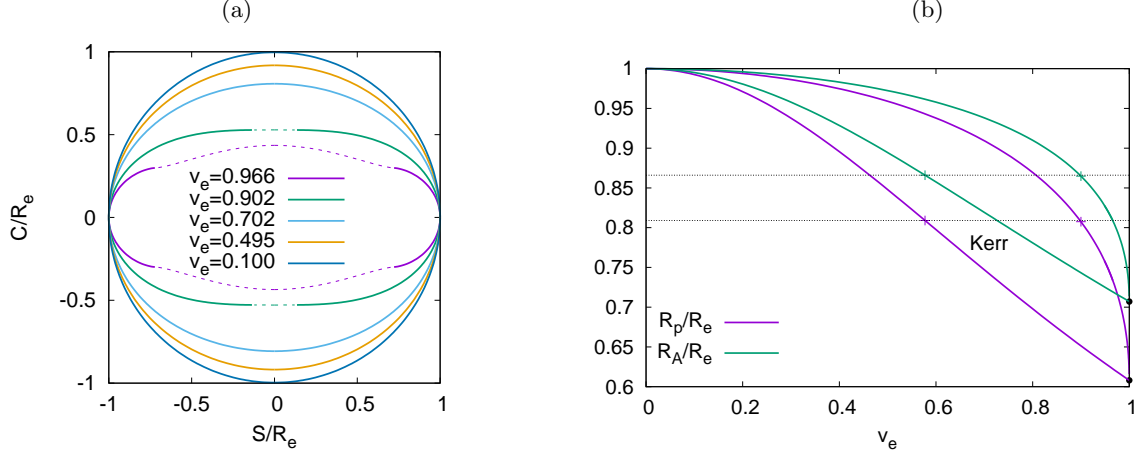


Figure 6: Properties of symmetric rotating wormholes at fixed equatorial throat radius R_e : (a) isometric embeddings of the hypersurface of the throat for rotational velocities $v_e = 0.966, 0.902, 0.702, 0.495,$ and 0.1 ; the dashed curves correspond to pseudo-Euclidean embedding. (b) The polar radius R_p/R_e and the areal radius R_A/R_e versus v_e . The crosses mark v_e^{cr} . For comparison the respective curves for the family of Kerr solutions are also shown.

a critical value of the rotational velocity v_e^{cr} their horizon can no longer be embedded in a Euclidean space, and a pseudo-Euclidean space must be used for the embedding [53, 54]. Since the family of rotating wormhole solutions approaches an extremal black hole, such a critical value of the rotational velocity v_e^{cr} is expected to arise for rotating wormholes as well.

To obtain the respective embedding, we equate the line element of the hypersurface $\eta = 0, t = 0$ with the (pseudo-)Euclidean line element

$$ds^2 = e^{-f+\nu} h d\theta^2 + e^{-f} h \sin^2 \theta d\phi^2 = d\rho^2 + \rho^2 d\phi^2 + dz^2 \quad (59)$$

with $\rho = S(\theta), z = C(\theta)$. Now comparison yields

$$\left(\frac{dS}{d\theta}\right)^2 \pm \left(\frac{dC}{d\theta}\right)^2 = e^{-f+\nu} h, \quad S^2 = e^{-f} h. \quad (60)$$

We show such embedding diagrams in Fig. 6 for the same set of wormholes with rotational velocities $v_e = 0.5, 0.7, 0.9,$ and 0.95 . The critical value corresponds to $v_e^{cr} = 0.9$ and marks the onset of a negative Gaussian curvature at the poles. Beyond v_e^{cr} parts of the hypersurface must be embedded in pseudo-Euclidean space, which is represented by the dashed curves in the figure.

We complete this demonstration of the throat geometry by considering the dependence of the throat radii on the rotational velocity v_e . We show in Fig. 6 the ratio of the polar radius to the equatorial radius R_p/R_e for fixed equatorial throat radius $R_e = 2$. As one would expect, this ratio decreases monotonically with increasing rotation, and reaches the corresponding ratio of radii of the extremal Kerr horizon in the limit $v_e \rightarrow 1$. The critical value v_e^{cr} , where the Gaussian curvature at the poles turns negative, is indicated by a cross in the figure. For comparison, also the respective curve for the Kerr solutions is shown. Interestingly, while the critical velocity $v_e^{cr} = 0.577$ is much smaller for the Kerr solution, the ratio R_p/R_e has the same value for the wormhole and the Kerr critical velocities, as indicated in the figure by a thin horizontal line. The figure also exhibits the ratio of the areal radius to the equatorial radius R_A/R_e , where the analogous findings hold.

Let us finally address the ergoregion of rotating wormholes. The ergoregion is defined by the condition $g_{tt} \geq 0$,

$$g_{tt} = -e^f + e^{-f} h \sin^2 \theta \omega^2 \geq 0, \quad (61)$$

where the equality defines the ergosurface. Inspection of the rotating wormhole solutions reveals, that the location of the ergosurface η_{ergo} in the equatorial plane is closely related to the angular velocity ω_0 of the throat. Indeed, the relation $\arctan(\eta_{\text{ergo}}/\eta_0) = \arccos(2\omega_0)$ holds with high accuracy. This is demonstrated in Fig 7.

For wormholes to possess an ergoregion in that part of the spacetime, where $\eta \geq 0$, which we have chosen to be asymptotically flat, they must rotate sufficiently fast. Note that the condition for the ergosphere at the throat in the equatorial plane can be written as

$$g_{tt} = -e^{f(0,\pi/2)} + e^{-f(0,\pi/2)} \eta_0^2 \omega_0^2 = 0 \iff -\frac{\eta_0^2}{R_e^2} (1 - R_e v_e)(1 + R_e v_e) = 0, \quad (62)$$

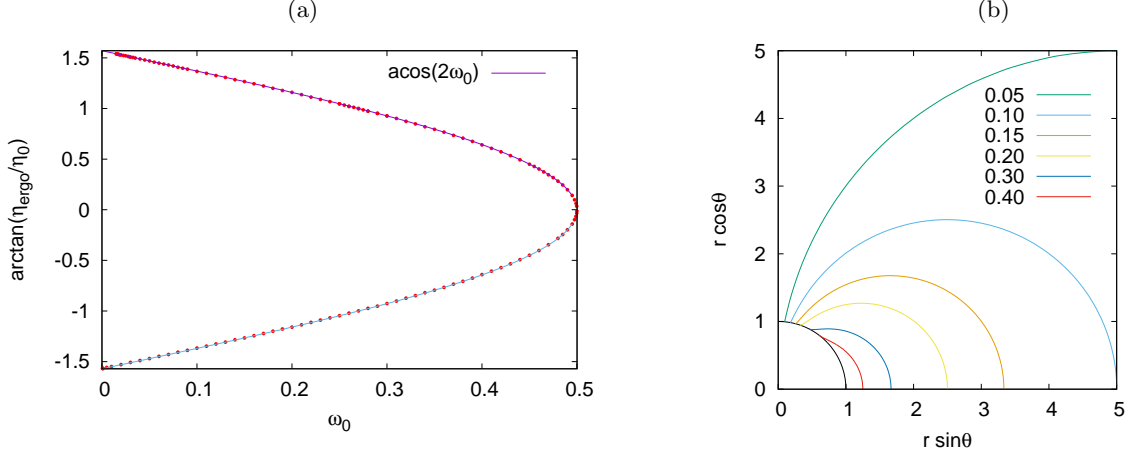


Figure 7: Properties of symmetric rotating wormholes at fixed throat parameter $\eta_0 = 1$: (a) the location of the ergosurface η_{ergo} in the equatorial plane is shown versus the angular velocity of the throat ω_0 and compared to the function $\arccos(2\omega_0)$; (b) one quadrant of the ergosurface and the throat in coordinates $r = \sqrt{\eta^2 + \eta_0^2}$ and θ for fixed ϕ and several values of ω_0 .

which yields $R_e = 2$ for $v_e = 1/2$. Thus the throat must rotate with half the velocity of light. As the rotation velocity v_e increases beyond this value, the ergoregion in this part of the spacetime increases. This is demonstrated in Fig. 7, where the ergosurfaces for increasing values of v_e and thus decreasing values of ω_0 are exhibited. However, there is always an ergoregion in the other part of the spacetime, where $\eta \leq 0$, and the function ω tends asymptotically to a finite value.

E. Geodesics

We now analyze the motion of particles and light in these rotating wormhole spacetimes. Interesting aspects emerging from this analysis are that massive particles can have stable bound states in rotating wormhole spacetimes. Moreover, there are unstable bound states for massless particles which indicates the presence of a photon region.

The motion of particles and light is governed by the Lagrangian \mathcal{L}

$$2\mathcal{L} = g_{\mu\nu} \dot{x}^\mu \dot{x}^\nu = \varepsilon, \quad (63)$$

where the dot denotes the derivative with respect to an affine parameter, and $\varepsilon = -1$ for particles and zero for light. The symmetries of the spacetime lead to two cyclic coordinates and thus two constants of motion, the energy E and the angular momentum L .

Let us for simplicity consider only motion in the equatorial plane, $\theta = \pi/2$. The Lagrangian then simplifies to

$$2\mathcal{L} = -e^f \dot{t}^2 + e^{-f} \left(e^\nu \dot{\eta}^2 + h \left(\dot{\phi} - \omega \dot{t} \right)^2 \right) = \varepsilon, \quad (64)$$

and the conserved charges become

$$E = \dot{t} (e^f - e^{-f} h \omega^2) + e^{-f} h \omega \dot{\phi}, \quad L = -e^{-f} h \omega \dot{t} + e^{-f} h \dot{\phi}. \quad (65)$$

Solving these equations for \dot{t} and $\dot{\phi}$ yields

$$\dot{t} = e^{-f} (E - \omega L), \quad \dot{\phi} = e^{-f} \left(\omega (E - \omega L) + e^{2f} \frac{L}{h} \right). \quad (66)$$

Insertion of these expressions into the Lagrangian leads to

$$e^{-f} e^\nu \dot{\eta}^2 - e^{-f} \left((E - \omega L)^2 - e^{2f} \frac{L^2}{h} \right) = \varepsilon. \quad (67)$$

When solving this equation for $\dot{\eta}^2$, it is instructive to introduce effective potentials V_{eff}^\pm as follows

$$\dot{\eta}^2 = e^{-\nu} (E - V_{\text{eff}}^+(L, \eta)) (E - V_{\text{eff}}^-(L, \eta)) = \Xi(\eta), \quad (68)$$

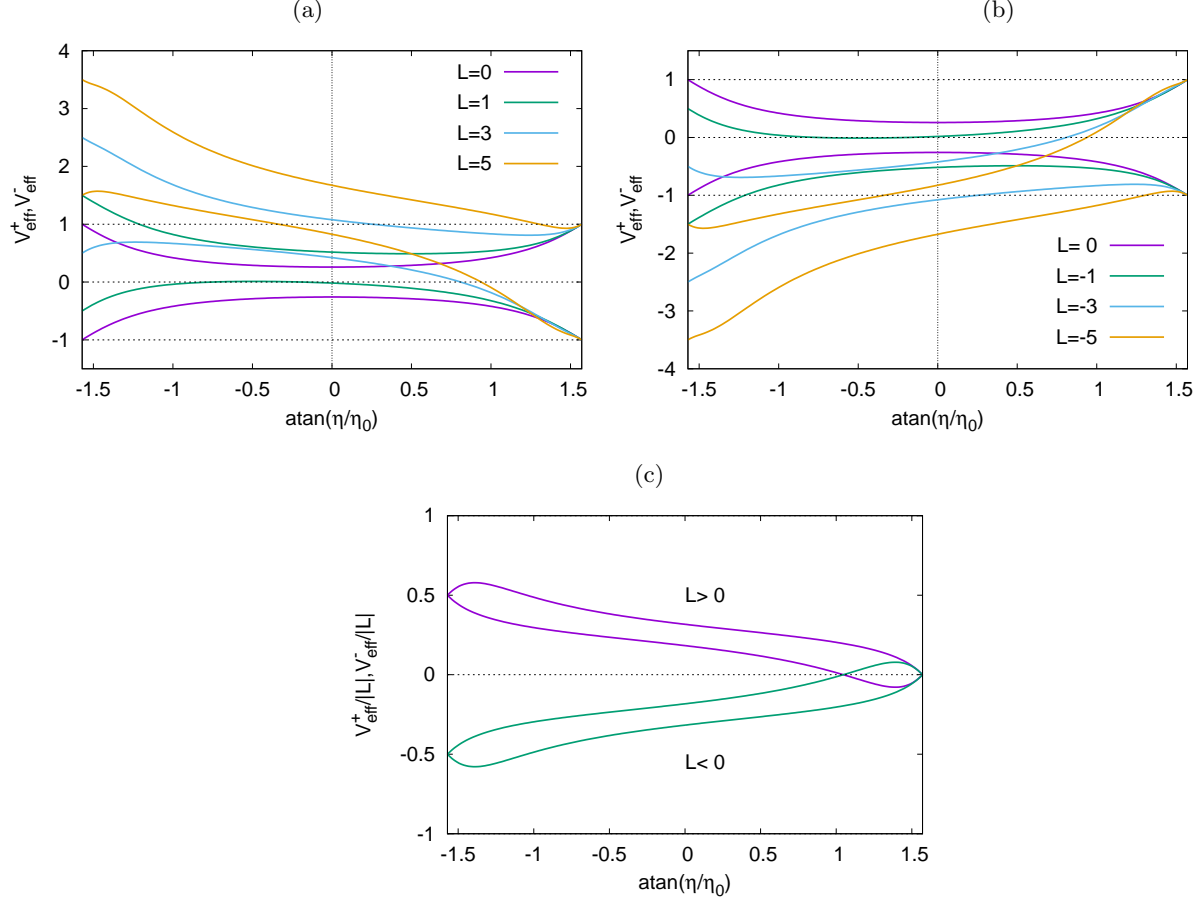


Figure 8: Geodesics of symmetric rotating wormholes at fixed equatorial throat radius $R_e = 2$: effective potentials V_{eff}^{\pm} for wormholes with rotational velocity $v_e = 0.78$ versus the compactified radial coordinate $\text{arctan}(\eta/\eta_0)$ for prograde motion (a) and retrograde motion (b) for several values of the angular momentum L of a massive particle. (c) $V_{\text{eff}}^{\pm}/|L|$ for massless particles for prograde and retrograde motion.

where we abbreviated the right hand side by $\Xi(\eta)$, and

$$V_{\text{eff}}^{\pm} = \omega L \pm \sqrt{e^{2f} \frac{L^2}{h} - \varepsilon e^f} \quad (69)$$

implying $V_{\text{eff}}^+(L, \eta) \geq V_{\text{eff}}^-(L, \eta)$. In fact the condition $\eta^2 = \Xi(\eta) \geq 0$ leads to a restriction for the allowed energies and angular momenta of the particles, $E \geq V_{\text{eff}}^+(L, \eta)$ or $E \leq V_{\text{eff}}^-(L, \eta)$.

Thus the study of these effective potentials allows for a classification of the possible orbits in the equatorial plane. We exhibit in Fig. 8 examples of the effective potentials for massive and massless particles. In particular, we observe that there are bound orbits of massive particles in such rotating wormhole spacetimes. This is in contrast to the static Ellis wormhole, which does not possess bound orbits. For rotating wormholes there are even three types of bound orbits, those that always remain within a single universe, those that oscillate between the two universes, and those that remain at the throat ($L = 0$ only). Two examples of such single universe bound orbits for a massive particle are shown in Fig. 9 together with a two-world bound orbit.

For the case of massless particles the effective potentials shown in Fig. 8 are divided by the modulus of the angular momentum. We note that V_{eff}^+ possesses a local maximum for retrograde motion for $\eta > 0$. This indicates that there is a photon region in this asymptotically flat universe. V_{eff}^+ additionally possesses a local maximum for prograde motion for $\eta < 0$, which indicates the presence of a photon region in the other universe, as well. However, whereas the motion there looks like prograde motion in our coordinates, where the $\eta > 0$ universe is asymptotically flat, it corresponds to retrograde motion, when an appropriate coordinate transformation is performed, making the $\eta < 0$ universe asymptotically flat.

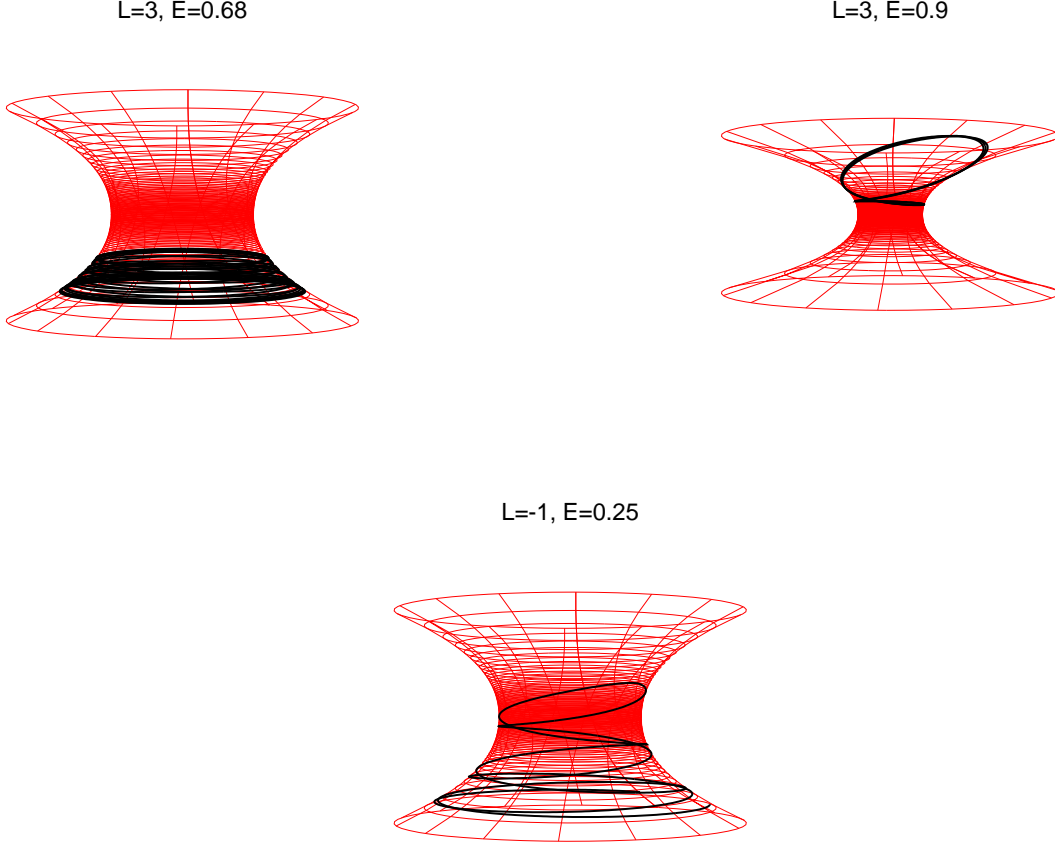


Figure 9: Geodesics of symmetric rotating wormholes at fixed equatorial throat radius R_e : embedding diagrams of bound orbits of a massive test particle in the equatorial plane of a symmetric fast rotating wormhole ($v_e = 0.78$) for several values of the particle energy E and angular momentum L .

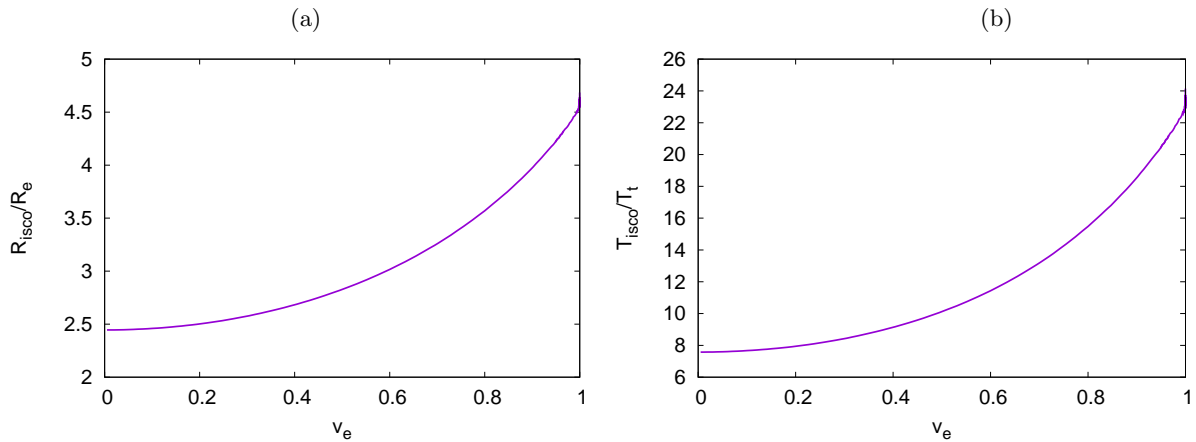


Figure 10: Geodesics of symmetric rotating wormholes at fixed equatorial throat radius R_e : the ratio R_{ISCO}/R_e of the ISCO radius to the throat radius (a) and the corresponding ratio of the orbital period T_{ISCO}/T_e (b) for retrograde motion of massive particles in the equatorial plane versus the rotational velocity v_e of the throat in the equatorial plane.

Of particular interest are the innermost stable circular orbits (ISCOs). To find the circular orbits we need to solve for $\Xi(\eta_{\text{CO}}) = \Xi'(\eta_{\text{CO}}) = 0$, while stability requires at the same time $\Xi''(\eta_{\text{CO}}) < 0$. ISCOs are then characterized by the change of stability, i. e., $\Xi''(\eta_{\text{ISCO}}) = 0$. For these rotating wormholes there are both corotating and counterrotating

ISCOs, just like for the Kerr black holes. Whereas the ISCO of the corotating orbits resides at the throat, the location of the ISCO of the counterrotating orbits depends on the rotation velocity. Here the ratio R_{ISCO}/R_e increases almost by a factor of two from the static limit to the limiting extremal Kerr black hole, as seen in Fig. 10. The figure also displays the ratio of the orbital period T_{ISCO}/T_e , where T_e denotes the orbital period of the throat (or the horizon of the extremal black hole), which increases roughly by a factor of three from the static limit to the extremal Kerr black hole.

IV. NON-SYMMETRIC WORMHOLES

We now turn to the discussion of the properties of non-symmetric rotating Ellis wormholes. In the non-symmetric case for fixed η_0 the wormhole solutions depend on two parameters, γ and $\omega_{-\infty}$. By varying these, the domain of existence can be mapped out. In the following we will first discuss the global charges of these non-symmetric rotating wormholes, and subsequently we will address their geometry.

A. Global Properties

Let us start our discussion of the properties of non-symmetric rotating wormholes with their global properties mass μ_+ , angular momentum J_+ and scalar charge D , obtained from the asymptotic expansion at $\eta \rightarrow \infty$. To demonstrate these properties, we fix the throat parameter $\eta_0 = 1$ and consider families of solutions, where the remaining two parameters γ and $\omega_{-\infty}$ are varied.

In Fig. 11a we exhibit the mass μ_+/R_e scaled by the equatorial throat radius versus the squared scalar charge D^2 for several fixed values of the parameter γ in the range $-4 \leq \gamma \leq 4$, where the negative values of γ are indicated in the figure by dots. The curves are obtained by varying the value of $\omega_{-\infty}$ for a fixed value of γ , starting from the static case $\omega_{-\infty} = 0$.

The symmetric static solution has vanishing mass and scalar charge $D = 1$, while the mass of the rotating solutions increases monotonically towards the mass of the limiting extremal Kerr black hole as the scalar charge decreases monotonically to zero. As seen in the figure, for fixed γ and fixed equatorial throat radius R_e , the mass always increases monotonically from the corresponding static value to the extremal Kerr value, while the scalar charge decreases monotonically to zero. In particular, for negative γ the mass is always positive. This is in contrast to positive γ , where the mass becomes negative in a part of the domain of existence. However, independent of γ , all families of non-symmetric wormhole solutions approach the extremal Kerr solution.

When we consider the angular momentum J_+/R_e^2 scaled by the squared equatorial throat radius, exhibited in Fig. 11b versus the squared scalar charge D^2 , we see the same monotonic behavior from the static solutions towards the limiting extremal Kerr black hole. The surprise encountered here, is that for a given scalar charge the value of the scaled angular momentum does not depend on the sign of γ .

To map the domain of existence it is favorable to consider the scaled scalar charge D/R_e (instead of D^2). The scaled mass μ_+/R_e and the scaled angular momentum J_+/R_e^2 are shown versus D/R_e in Figs. 11 (c) and (d), respectively. The scaled mass is then located in a thin band, reaching to large values of D/R_e for large positive values of γ , while shrinking towards the extremal Kerr limit for large negative values of γ . The scaled angular momentum J_+/R_e^2 on the other hand now distinguishes between positive and negative values of γ , when considered versus D/R_e . Fig. 11e finally shows the scaled mass μ_+/R_e versus the scaled angular momentum J_+/R_e^2 . Here the limiting behavior of the scaled mass for large negative γ can be anticipated, which corresponds to $\mu_+/R_e \rightarrow 1$.

To demonstrate the dependence on the parameter $\omega_{-\infty}$, we exhibit in Fig. 12 the mass μ_+ (a), the angular momentum J_+ (b), the squared scalar charge D^2 (c), and the coefficient Eq. (28) $c_2 = \mu_+^2 + \eta_0^2 - D^2$ (d) versus the parameter γ for fixed values of the parameter $\omega_{-\infty}$ in the range $0 \leq \omega_{-\infty} \leq 5$. Recall, that $\gamma = 0$ represents the symmetric case, while $\omega_{-\infty} = 0$ represents the static case. Again the asymmetry between positive and negative values of γ is evident.

As a final point of interest concerning the global charges, let us consider the mass μ_+ versus the angular momentum J_+ for fixed scalar charge D , exhibited in Fig. 13a, where D is varied in the range $0.6 \leq D \leq 2$. The corresponding values of the parameters $\omega_{-\infty}$ and γ are shown in Fig. 13b. Here we observe an interesting bifurcation phenomenon, where the critical value corresponds to $D_{\text{cr}} = 1$. For a given value of $D < D_{\text{cr}}$, there are two M curves, located symmetrically w.r.t. J_+ , which end at respective limiting values. As D increases towards D_{cr} , the two curves approach each other closer and closer, until at D_{cr} the two curves cross. This happens precisely at $\mu_+ = J_+ = 0$. For $D > D_{\text{cr}}$, the pattern changes, and there emerge a higher mass curve and a low mass curve. The figure also exhibits two thin dotted curves, which delimit the domain of existence.

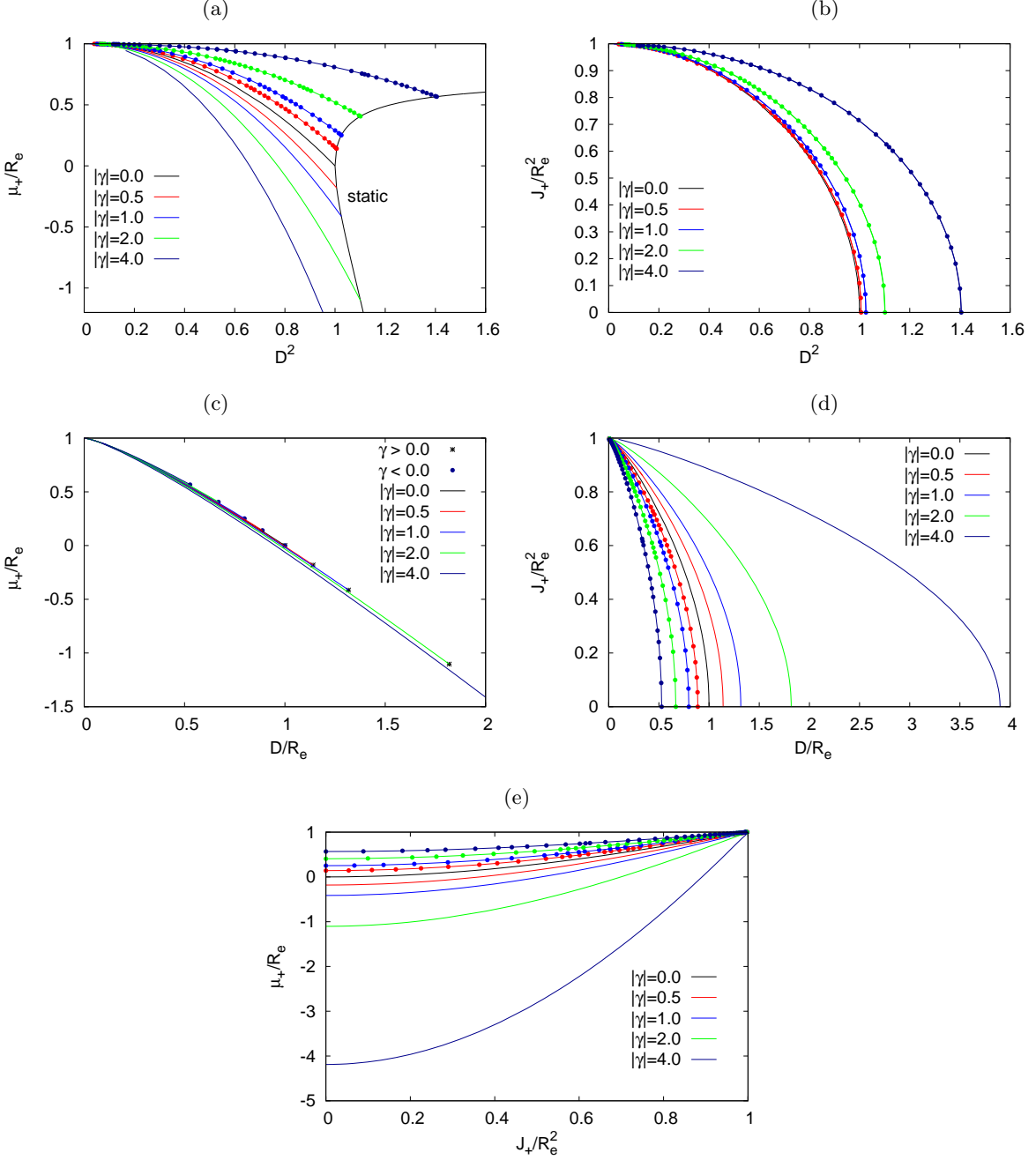


Figure 11: Properties of non-symmetric rotating wormholes at fixed throat parameter $\eta_0 = 1$: (a) the mass μ_+/R_e scaled by the equatorial throat radius versus the squared scalar charge D^2 , (b) same as (a) for the angular momentum J_+/R_e^2 scaled by the squared equatorial throat radius, (c) the scaled mass μ_+/R_e versus the scaled scalar charge D/R_e , (d) the scaled angular momentum J_+/R_e^2 versus the scaled scalar charge D/R_e , (e) the scaled mass μ_+/R_e versus the scaled angular momentum J_+/R_e^2 . The parameter γ is varied in the range $-4 \leq \gamma \leq 4$ with negative values indicated by dots.

B. Velocity of the throat

When the throat has angular velocity $\Omega = \omega_0$, its rotational velocity in the equatorial plane is given by $v_e = R_e \Omega$. As seen in the previous section, symmetric wormholes always satisfy $v_e \leq 1$. This continues to hold for non-symmetric rotating wormholes with negative values of γ . However, non-symmetric rotating wormholes with positive values of γ can exceed this bound. This is seen in Fig. 14a, where we exhibit the rotational velocity v_e versus the square of the scalar charge, D^2 , for several families of non-symmetric rotating wormholes, characterized by fixed values of the

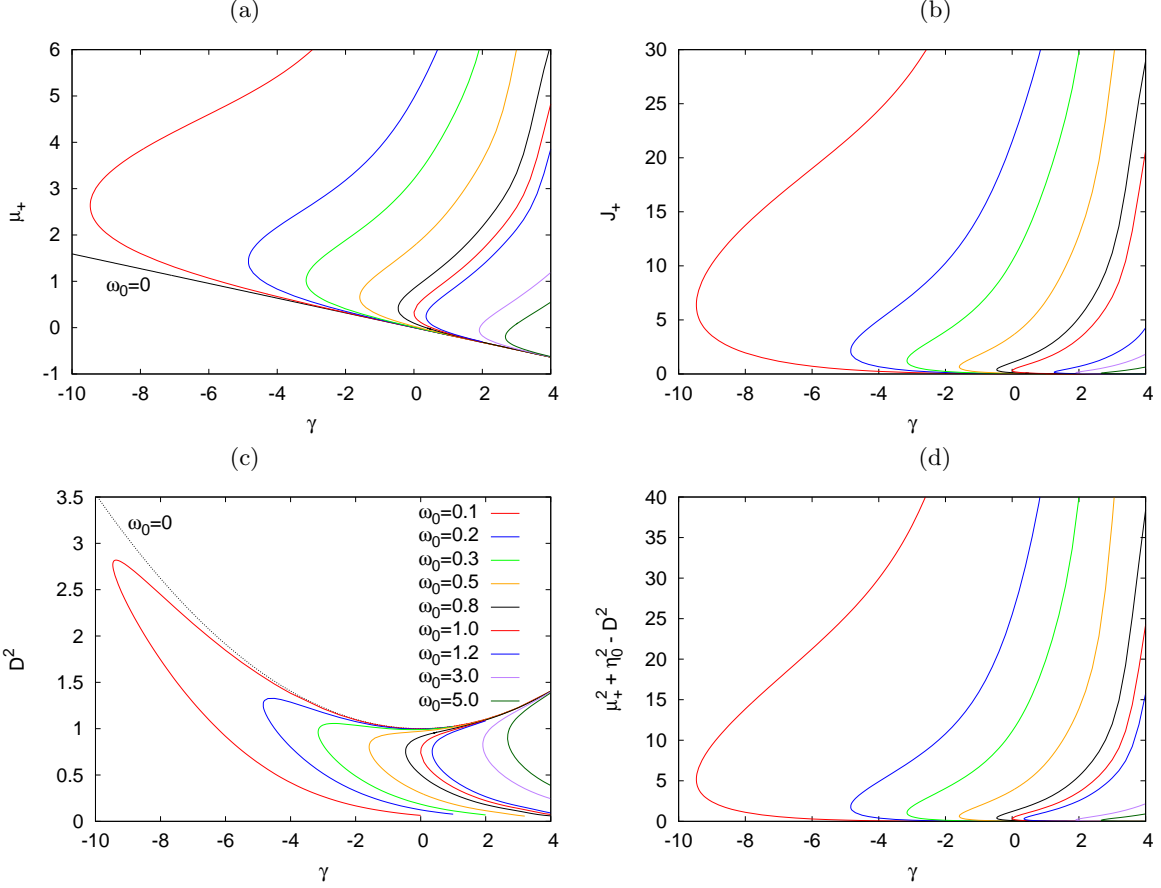


Figure 12: Properties of non-symmetric rotating wormholes at fixed throat parameter $\eta_0 = 1$: (a) the mass μ_+ , (b) the angular momentum J_+ (c) the squared scalar charge D^2 , and (d) the coefficient $c_2 = \mu_+^2 + \eta_0^2 - D^2$ versus γ . The parameter $\omega_{-\infty}$ is varied in the range $0 \leq \omega_{-\infty} \leq 5$.

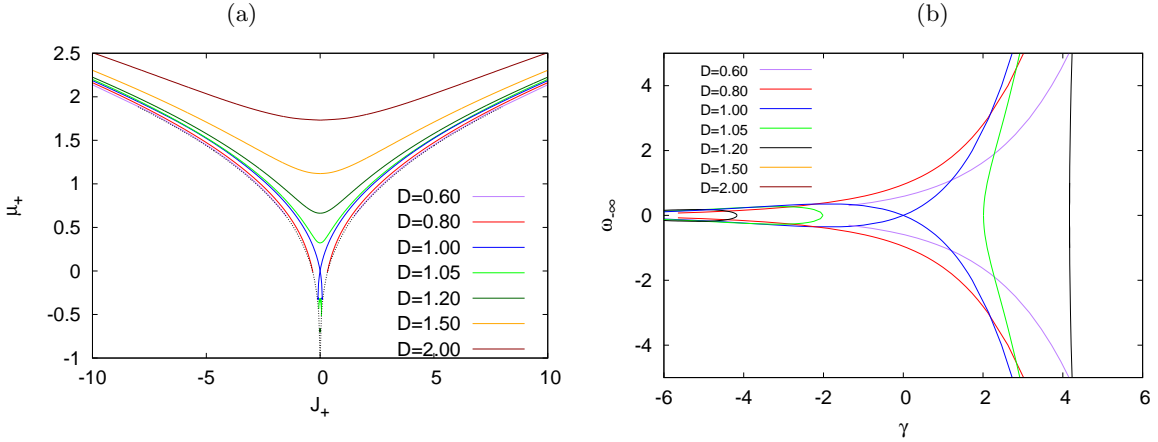


Figure 13: Properties of non-symmetric rotating wormholes at fixed throat parameter $\eta_0 = 1$: (a) the mass μ_+ versus the angular momentum J_+ , (b) the parameter $\omega_{-\infty}$ versus the parameter γ . The scalar charge D is varied in the range $0.6 \leq D \leq 2$. The thin dotted curves in (a) delimit the domain of existence.

parameter γ .

Since the rotational velocity v_e of the extremal Kerr black hole precisely saturates the bound, $v_e = 1$, and since all families of non-symmetric rotating wormholes possess the extremal Kerr black hole as their limiting configuration, the quantity v_e does no longer possess a monotonic behavior for the families of rotating wormholes with fixed $\gamma > 0$. Consequently, v_e is no longer the quantity of choice to demonstrate the physical properties of non-symmetric rotating

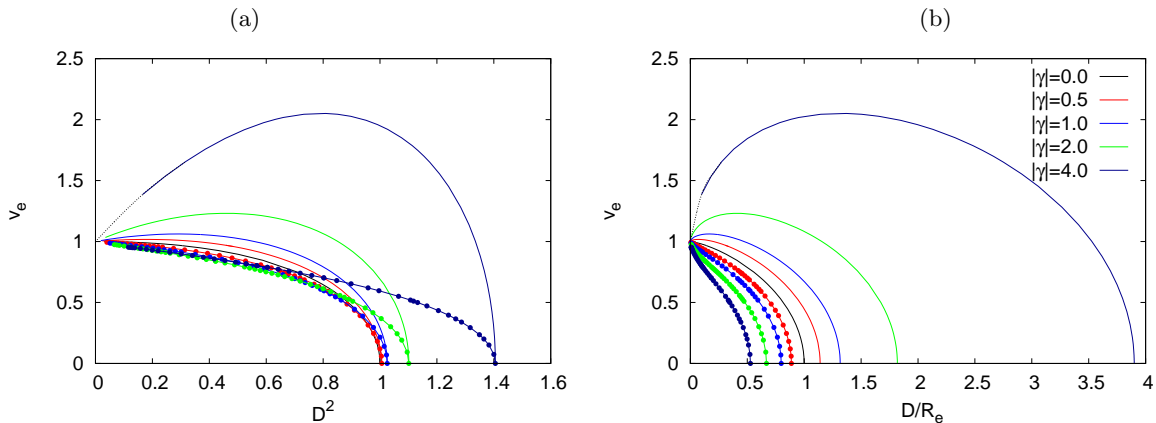


Figure 14: Properties of non-symmetric rotating wormholes at fixed throat parameter $\eta_0 = 1$: the rotational velocity in the equatorial plane $v_e = R_e \Omega$ versus the squared scalar charge D^2 (a) and versus the scaled scalar charge D/R_e (b). The parameter γ is varied in the range $-4 \leq \gamma \leq 4$ with negative values indicated by dots. The thin dotted lines correspond to extrapolations towards the limiting extremal Kerr black hole.

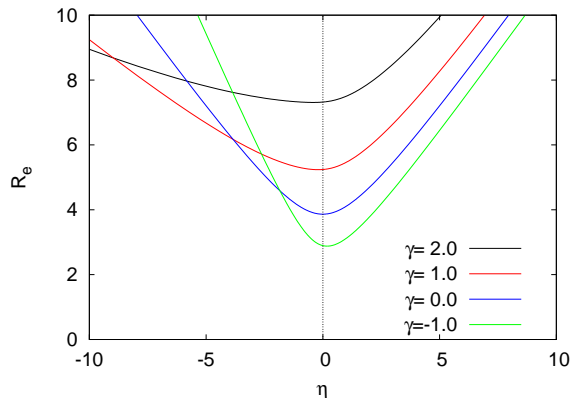


Figure 15: Properties of non-symmetric rotating wormholes at fixed throat parameter $\eta_0 = 1$: the equatorial radius R_e versus the radial coordinate η for spacetimes with $\omega(-\infty) = 0.5$ (on the upper branch) and $\gamma = f(-\infty) = 2.0, 1.0, 0.0$ and -1.0 . The minimal value of R_e represents the respective location of the throat.

wormholes. In this case the scalar charge, squared or scaled, represents a preferable physical parameter, since it always changes monotonically. The rotational velocity v_e is shown versus the scaled scalar charge, D/R_e , in Fig. 14b.

Let us now address the origin of the fact, that the rotational velocity v_e exceeds the speed of light, i.e., $v_e > 1$, for $\gamma > 0$ wormholes in a part of their parameter space adjoining the extremal Kerr black hole. For those wormholes the metric function ω , whose value at the throat enters the expression for the rotational velocity v_e , increases strongly towards the throat, assuming very large values at the throat (and even larger values beyond the throat). At the same time, the metric coefficient g_{00} is monotonically decreasing from its asymptotic value of $g_{00}(\infty) = -1$ to large negative values at the throat. (Note, that we exhibit examples of the metric functions for such wormholes in the Appendix.) Thus the wormholes exhibit strong antigravitational features, which are mainly associated with their negative mass. Consequently time is running much faster for an observer at the throat than for an observer far from the wormhole. For an observer close to the throat the rotational velocity v_e never exceeds the speed of light.

C. Location of the throat

Let us next address the throat of these non-symmetric rotating wormholes. In particular, we would like to know, where we find the throat in the equatorial plane, i.e., at which coordinate η_e it is located there, and whether the throat coordinate η_t depends on the polar angle θ . To approach the first question, we show in Fig. 15 examples of the equatorial radius R_e versus the radial coordinate η for several wormhole solutions. These spacetimes are

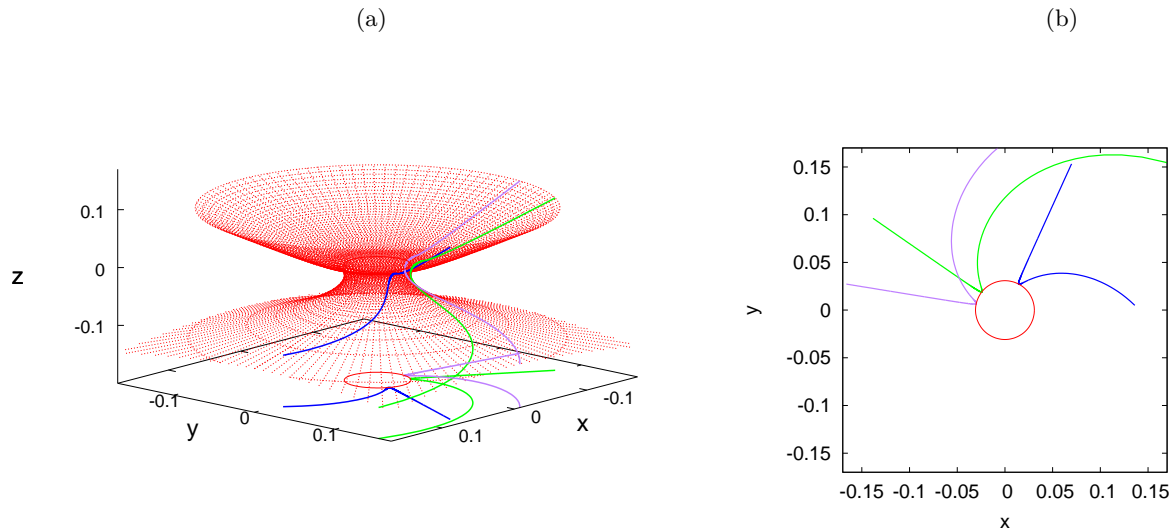


Figure 16: Geodesics of non-symmetric rotating wormholes: massless particles with zero angular momentum starting at coordinates $x_0 = 0.136, 0.335, 0.399$ and $y_0 = 0$ on the second manifold, passing through the throat for a wormhole solution with $\omega_{-\infty} = 1000$, $\gamma = 10.008$. Embedding diagram (a) and projection in the equatorial plane (b).

characterized by the parameter value $\omega(-\infty) = 0.5$ (located on the upper branch) and the values of the asymmetry parameter $\gamma = f(-\infty) = 2.0, 1.0, 0.0$ and -1.0 . Their scalar charge is given by $D = 0.33984, 0.43155, 0.55277$, and 0.71636 , respectively.

The location η_e of the throat in the equatorial plane is given by the minimum of the equatorial radius R_e . We note that the location of the throat η_e depends only weakly on the parameter γ in the considered range, $-1 \leq \gamma \leq 2$. For negative γ the throat is located at small positive η_e , while for positive γ it resides at small negative η_e . We observe that, in contrast to the throat location η_e , the throat radius R_e depends strongly on γ , and increases with increasing γ .

In Boyer-Lindquist coordinates, the event horizon of a rotating black hole is characterized by a single value of the radial coordinate. Likewise, the throat of a symmetric rotating wormhole is characterized by a single value of the radial coordinate. Let us now see, whether an analogous result holds for the throat of a non-symmetric rotating wormhole. To that end we analyze the coordinates of the minimal surface defining the throat. In particular, we calculate the value of the radial throat coordinate η_t as a function of the polar angle θ , and find only a very slight dependence of η_t on θ . For instance, the ratio η_t/η_e is always very close to one, with deviations less than 0.1% and thus within the numerical accuracy. While we cannot answer, whether η_t is indeed a constant, we can state that a constant η_t represents at least a good approximation. From a geometrical point of view, however, the throat is highly deformed for a fast rotating wormhole.

D. Geodesics

As our last quest let us address the trajectories of particles and light in these non-symmetric rotating wormhole spacetimes. As in the symmetric case we find stable bound orbits of massive particles and unstable bound orbits of massless particles. However, we now focus on the orbits of particles in wormhole spacetimes, whose equatorial throat velocity v_e exceeds the speed of light, since this is a new phenomenon as compared to the symmetric case. As an example, we exhibit in Fig. 16 the orbits of massless particles with zero angular momentum starting at the coordinates $x_0 = 20, 50, 60$ on the second manifold, which pass through the throat of a wormhole solution with parameters $\omega_{-\infty} = 1000$, $\gamma = 10.008$, and $v_e \approx 8$. Fig. 16a shows the orbits in an embedding of the wormhole spacetime, while Fig. 16b gives a projection of the orbits in the equatorial plane.

In such a spacetime the particle orbits appear rather strange at first sight. Moving with zero angular momentum in the negative η region towards the throat, the particle orbits are strongly dragged along by the rapidly rotating space time until the particles pass the throat. Beyond the throat the particles then follow more or less straight lines, as they move across the positive η region towards infinity. In this region the function ω decreases rapidly outside the throat and vanishes asymptotically. So the dragging of the radial geodesics diminishes fast, when away from the throat.

V. CONCLUSIONS

The construction of Lorentzian rotating wormholes, which are generalizations of the Ellis wormholes, has been a challenge for a very long time. With this study we have provided the first detailed investigation of rotating Ellis wormholes in General Relativity. These wormhole solutions are supported by a phantom field, and can be either symmetric or non-symmetric. Whereas the static solutions are known in closed form, the non-perturbative rotating wormholes have been obtained by numerical integration of the coupled system of Einstein-phantom equations, subject to appropriate boundary conditions. The latter guarantee that the solutions are globally regular and asymptotically flat on one side, while for the second side a coordinate transformation is necessary to achieve asymptotic flatness.

The global charges of the wormhole solutions can be obtained from their asymptotic expansions. For symmetric wormholes the mass is the same on both sides of the wormhole. The same holds true for the angular momentum. However, this is no longer the case, when the asymmetry parameter γ differs from zero. The throat of symmetric wormholes resides at the center of our coordinate system, where the radial coordinate η is zero. The corresponding surface represents a minimal surface, which changes from a round sphere in the static limit to a strongly deformed axially symmetric surface with negative Gaussian curvature at the poles, when the rotational velocity becomes sufficiently high. For non-symmetric wormholes the minimal surface defining the throat may still be described by a surface of constant radial coordinate η (at least within our numerical accuracy). But, depending on the sign of the asymmetry parameter γ , the location of the throat is shifting towards positive or negative values of η .

Many of the properties revealed by our calculations are rather surprising, for instance,

- rotating wormholes satisfy a Smarr type relation,
- rotating wormholes possess an extremal Kerr black hole as limiting configuration,
- for rotating wormholes the crossing from positive to negative Gaussian curvature at the poles of the throat occurs precisely at the same ratio of radii as for Kerr black holes,
- the dimensionless quadrupole moment of rotating wormholes can strongly exceed the Kerr value,
- the ergoregion of the rotating wormholes is very different from the expectations raised by the Teo wormhole,
- non-symmetric wormholes can possess a rotational velocity of the throat which exceeds the speed of light,
- unlike the static Ellis wormholes, the rotating wormholes do possess bound orbits.

Furthermore, we conjecture that the observations that (i) the violation of the NEC decreases with increasing global charge, while (ii) the wormholes approach an extremal black hole solution as a limiting configuration, represent generic features of wormholes. For the present study, the global charge is angular momentum, and the extremal black hole corresponds to a Kerr black hole. As shown before, electrically charged static Ellis wormholes in four dimensions approach with increasing charge in an analogous fashion an extremal Reissner-Nordström black hole [51], while rotating wormholes (with equal angular momenta) in five dimensions tend with increasing angular momenta towards the corresponding extremal Myers-Perry black hole [50].

So far we have not addressed the important issue of the stability of these rotating wormhole solutions. It has been shown before, that the static Ellis wormholes are unstable, both in four [55–57] (see also [58]) and higher dimensions [59]. On the other hand, arguments have been given which indicate that wormholes might be stabilized by rotation [60]. Indeed, in the case of five-dimensional rotating wormholes it has been shown, that the unstable mode of the static solutions disappears, when the rotation is sufficiently fast [50]. We are planning to do the corresponding stability analysis also for four-dimensional rotating wormholes, to see whether rotation will eliminate the unstable mode as well in four dimensions. On the other hand, stability of wormholes could also be achieved, when the Einstein-Hilbert action of General Relativity is replaced by a more general action with higher curvature terms [22, 23].

Acknowledgments

We gratefully acknowledge support by the DFG within the Research Training Group 1620 “Models of Gravity” and by FP7, Marie Curie Actions, People, International Research Staff Exchange Scheme (IRSES-606096). We gratefully acknowledge discussions with E. Radu.

VI. APPENDIX

We here demonstrate the behaviour of the metric functions for asymmetric wormholes with rotational velocity $v_e > 1$. Fig. 17 exhibits the functions f (a), ν (b), ω (c) versus the compactified radial coordinate $\arctan(\eta/\eta_0)$ for a solution with parameters $\gamma = 10.008$, $\omega_{-\infty} = 1000$. The function f hardly deviates from the corresponding function of the static wormhole, and the function ν remains close to one. Still the function ω assumes very large values towards

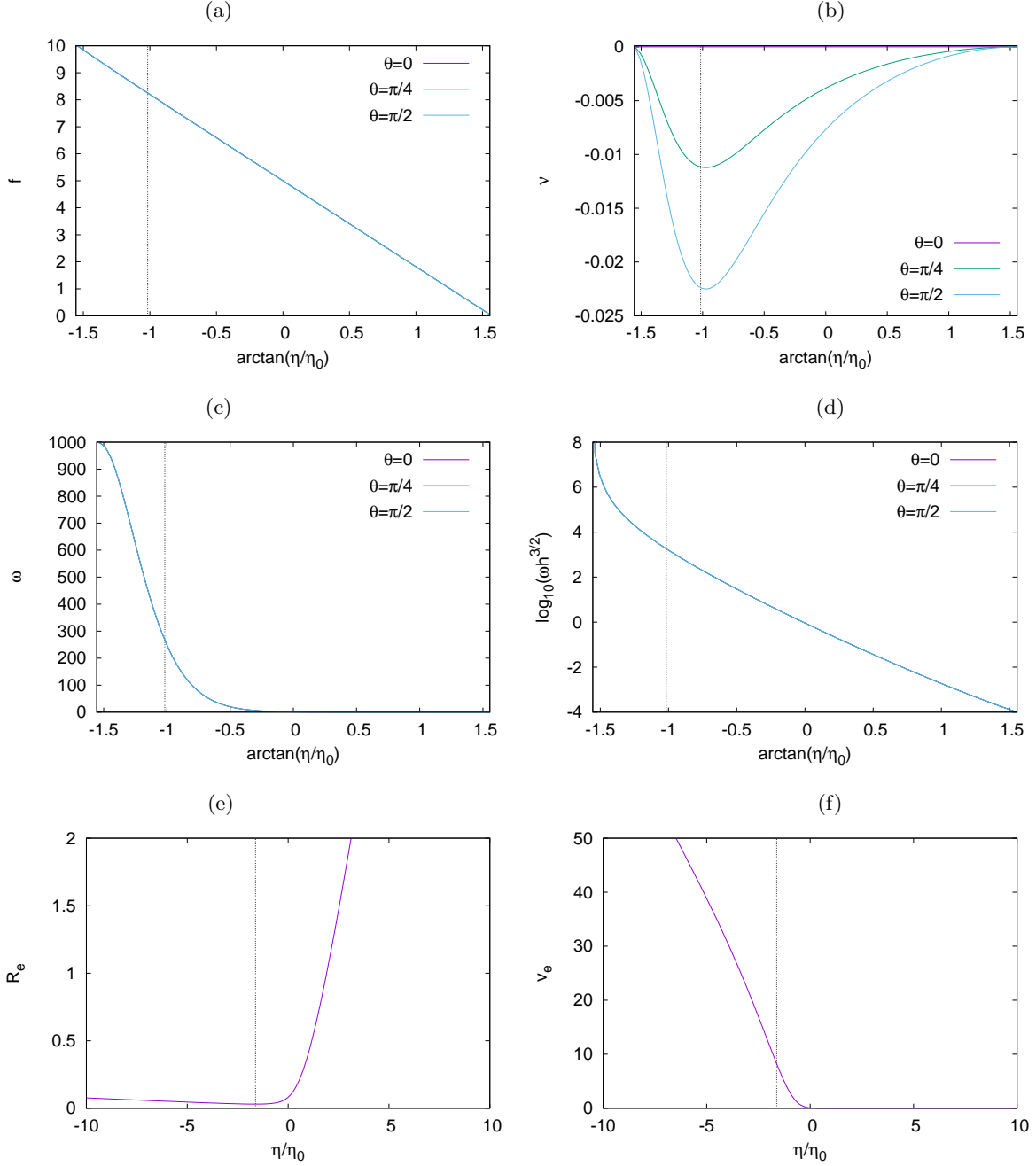


Figure 17: Non-symmetric rotating wormhole with $v_e > 1$: the metric functions f (a), ν (b), ω (c), the combination $\omega h^{3/2}$ (d), versus the compactified radial coordinate $\arctan(\eta/\eta_0)$, and the equatorial radius R_e (e) and the rotational velocity $v_e = R_e \omega$ (f) versus the scaled radial coordinate η/η_0 . The thin vertical line marks the location of the throat.

the throat and beyond the throat. The combination $\omega h^{3/2}$ is exhibited in (d) to demonstrate the fall-off of ω for $\eta \rightarrow +\infty$.

For this wormhole spacetime also the equatorial radius $R_e(\eta)$ (e) and the rotational velocity in the equatorial plane $v_e(\eta)$ (f) are shown versus the scaled radial coordinate η/η_0 , demonstrating that $v_e(\eta)$ exceeds the velocity of light

beyond a certain value of the radial coordinate.

-
- [1] For an overview see e. g. M. Visser, “Lorentzian wormholes: From Einstein to Hawking”, Woodbury, USA: AIP (1995) 412 p
- [2] A. Einstein and N. Rosen, Phys. Rev. **48** (1935) 73.
- [3] J. A. Wheeler, Annals Phys. **2**, 604-614 (1957).
- [4] J. A. Wheeler, *Geometrodynamics* (Academic, New York, 1962).
- [5] M. D. Kruskal, Phys. Rev. **119**, 1743-1745 (1960).
- [6] R. W. Fuller, J. A. Wheeler, Phys. Rev. **128**, 919-929 (1962).
- [7] I. H. Redmount, Prog. Theor. Phys. **73** (1985) 140.
- [8] D. M. Eardley, Phys. Rev. Lett. **33**, 442-444 (1974).
- [9] R. M. Wald, S. Ramaswamy, Phys. Rev. **D21**, 2736-2741 (1980).
- [10] H. G. Ellis, J. Math. Phys. **14**, 104-118 (1973).
- [11] H. G. Ellis, Gen. Rel. Grav. **10**, 105-123 (1979).
- [12] K. A. Bronnikov, Acta Phys. Polon. **B4**, 251-266 (1973).
- [13] T. Kodama, Phys. Rev. **D18**, 3529-3534 (1978).
- [14] M. S. Morris, K. S. Thorne, Am. J. Phys. **56**, 395-412 (1988).
- [15] M. S. Morris, K. S. Thorne and U. Yurtsever, Phys. Rev. Lett. **61**, 1446 (1988).
- [16] F. S. N. Lobo, Phys. Rev. D **71**, 084011 (2005) [gr-qc/0502099].
- [17] D. Hochberg, Phys. Lett. **B251**, 349-354 (1990).
- [18] H. Fukutaka, K. Tanaka, K. Ghoroku, Phys. Lett. **B222**, 191-194 (1989).
- [19] K. Ghoroku, T. Soma, Phys. Rev. **D46**, 1507-1516 (1992).
- [20] N. Furey, A. DeBenedictis, Class. Quant. Grav. **22**, 313-322 (2005) [gr-qc/0410088].
- [21] K. A. Bronnikov and E. Elizalde, Phys. Rev. D **81**, 044032 (2010) [arXiv:0910.3929 [hep-th]].
- [22] P. Kanti, B. Kleihaus and J. Kunz, Phys. Rev. Lett. **107**, 271101 (2011) [arXiv:1108.3003 [gr-qc]].
- [23] P. Kanti, B. Kleihaus and J. Kunz, Phys. Rev. D **85** (2012) 044007 [arXiv:1111.4049 [hep-th]].
- [24] F. Abe, Astrophys. J. **725**, 787 (2010) [arXiv:1009.6084 [astro-ph.CO]].
- [25] Y. Toki, T. Kitamura, H. Asada and F. Abe, Astrophys. J. **740**, 121 (2011) [arXiv:1107.5374 [astro-ph.CO]].
- [26] R. Takahashi and H. Asada, Astrophys. J. **768**, L16 (2013) [arXiv:1303.1301 [astro-ph.CO]].
- [27] J. G. Cramer, R. L. Forward, M. S. Morris, M. Visser, G. Benford and G. A. Landis, Phys. Rev. D **51**, 3117 (1995) [astro-ph/9409051].
- [28] V. Perlick, Phys. Rev. D **69**, 064017 (2004) [gr-qc/0307072].
- [29] N. Tsukamoto, T. Harada and K. Yajima, Phys. Rev. D **86**, 104062 (2012) [arXiv:1207.0047 [gr-qc]].
- [30] C. Bambi, Phys. Rev. D **87**, 107501 (2013) [arXiv:1304.5691 [gr-qc]].
- [31] P. G. Nedkova, V. K. Tinchev and S. S. Yazadjiev, Phys. Rev. D **88**, 124019 (2013) [arXiv:1307.7647 [gr-qc]].
- [32] M. Zhou, A. Cardenas-Avendano, C. Bambi, B. Kleihaus and J. Kunz, Phys. Rev. D **94**, 024036 (2016) [arXiv:1603.07448 [gr-qc]].
- [33] V. Dzhunushaliev, V. Folomeev, B. Kleihaus and J. Kunz, JCAP **1104**, 031 (2011) [arXiv:1102.4454 [astro-ph.GA]].
- [34] V. Dzhunushaliev, V. Folomeev, B. Kleihaus and J. Kunz, Phys. Rev. D **85**, 124028 (2012) [arXiv:1203.3615 [gr-qc]].
- [35] V. Dzhunushaliev, V. Folomeev, B. Kleihaus and J. Kunz, Phys. Rev. D **87**, 104036 (2013) [arXiv:1302.5217 [gr-qc]].
- [36] V. Dzhunushaliev, V. Folomeev, B. Kleihaus and J. Kunz, Phys. Rev. D **89**, 084018 (2014) [arXiv:1401.7093 [gr-qc]].
- [37] A. Aringazin, V. Dzhunushaliev, V. Folomeev, B. Kleihaus and J. Kunz, JCAP **1504**, 005 (2015) [arXiv:1412.3194 [gr-qc]].
- [38] V. Dzhunushaliev, V. Folomeev, B. Kleihaus and J. Kunz, JCAP **1608**, 030 (2016) [arXiv:1601.04124 [gr-qc]].
- [39] P. E. Kashargin and S. V. Sushkov, Grav. Cosmol. **14**, 80 (2008) [arXiv:0710.5656 [gr-qc]].
- [40] P. E. Kashargin and S. V. Sushkov, Phys. Rev. D **78**, 064071 (2008) [arXiv:0809.1923 [gr-qc]].
- [41] B. Kleihaus and J. Kunz, Phys. Rev. D **90**, 121503 (2014) [arXiv:1409.1503 [gr-qc]].
- [42] E. Teo, Phys. Rev. D **58**, 024014 (1998) [gr-qc/9803098].
- [43] R. P. Geroch, J. Math. Phys. **11**, 2580 (1970).
- [44] R. O. Hansen, J. Math. Phys. **15**, 46 (1974).
- [45] C. Hoenselaers and Z. Perjés, Class. Quant. Grav. **7**, 1819 (1990).
- [46] T. P. Sotiriou and T. A. Apostolatos, Class. Quant. Grav. **21**, 5727 (2004) [gr-qc/0407064].
- [47] G. Pappas and T. A. Apostolatos, Phys. Rev. Lett. **108**, 231104 (2012) [arXiv:1201.6067 [gr-qc]].
- [48] B. Kleihaus, J. Kunz, S. Mojica and M. Zagermann, Phys. Rev. D **93**, 064077 (2016) [arXiv:1601.05583 [gr-qc]].
- [49] B. Kleihaus and J. Kunz, Phys. Rev. Lett. **86**, 3704 (2001) [gr-qc/0012081].
- [50] V. Dzhunushaliev, V. Folomeev, B. Kleihaus, J. Kunz and E. Radu, Phys. Rev. D **88**, 124028 (2013) [arXiv:1309.2448 [gr-qc]].
- [51] O. Hauser, R. Ibadov, B. Kleihaus and J. Kunz, Phys. Rev. D **89**, 064010 (2014) arXiv:1312.3539 [gr-qc].
- [52] B. Kleihaus, J. Kunz and S. Mojica, Phys. Rev. D **90**, 061501 (2014) [arXiv:1407.6884 [gr-qc]].
- [53] L. Smarr, Phys. Rev. Lett. **30**, 71 (1973) Erratum: [Phys. Rev. Lett. **30**, 521 (1973)].
- [54] L. Smarr, Phys. Rev. D **7**, 289 (1973).

- [55] H. -a. Shinkai and S. A. Hayward, Phys. Rev. D **66**, 044005 (2002) [gr-qc/0205041].
- [56] J. A. Gonzalez, F. S. Guzman, and O. Sarbach, Class. Quant. Grav. **26**, 015010 (2009) [arXiv:0806.0608 [gr-qc]].
- [57] J. A. Gonzalez, F. S. Guzman, and O. Sarbach, Class. Quant. Grav. **26**, 015011 (2009) [arXiv:0806.1370 [gr-qc]].
- [58] R. A. Konoplya and A. Zhidenko, arXiv:1606.00517 [gr-qc].
- [59] T. Torii and H. a. Shinkai, Phys. Rev. D **88**, 064027 (2013) [arXiv:1309.2058 [gr-qc]].
- [60] T. Matos and D. Nunez, Class. Quant. Grav. **23**, 4485 (2006) [gr-qc/0508117].